Fault Diagnosis and Estimation in Inkjet Printers Using Self-Sensing Piezo Actuators

Master of Science Thesis

For the degree of Master of Science in Systems and Control at Delft University of Technology

Supervisors:

Delft University of Technology

P. Mohajerin Esfahani, Associate Professor

M.A. Sheikhi, MSc

Canon

Y.G.J. de Loore, MSc

P.J.B. Hacking, MSc

A. Amini

Faculty of Mechanical Engineering (ME)

Delft University of Technology

The writer was enabled by Canon Production Printing Netherlands B.V. to perform research that partly forms the basis for this report. Canon Production Printing B.V. does not accept responsibility for the accuracy of the data, opinions and conclusions mentioned in this report, which are entirely for the account of the writer.

Abstract

Diagnosing nozzle faults in high-end industrial printers, such as the ones developed by Canon Production Printing (CPP), remains challenging due to the interplay of fluid dynamics and mechanical actuation. These systems rely on self-sensing signals that are often subtle and nonlinear, complicating both detection and interpretation. However, accurate and timely diagnosis is essential to maintain print quality, minimize waste, and reduce maintenance effort. This thesis investigates hybrid fault diagnosis methods that integrate model-based and data-driven techniques to improve detection reliability and generalization, particularly for piezoelectric inkjet systems. Traditional fault detection approaches in this context often rely on rule-based thresholds applied to features extracted from self-sensing signals. Although these methods can be effective, they are typically sensitive to variations in operating conditions. In contrast, model-based techniques use simplified system dynamics to generate residual signals that reflect deviations from expected behavior. In this thesis, we propose a hybrid framework that addresses the Fault Detection and Isolation (FDI) problem from a frequency domain perspective. By learning from signal characteristics, the method avoids the need for manually defined thresholds and predefined reference signatures. Instead, it uses classifiers trained to distinguish between different fault types and improve the adaptability to unseen cases. Building on this framework, the second part of the thesis addresses Fault Estimation (FE), aiming to reconstruct how faults evolve over time. A linear model-based estimation scheme is developed in both discrete-time and continuous-time forms. Even though this approach simplifies certain nonlinear dynamics, it provides useful fault tracking results, particularly for moderate fault levels. The evaluation on synthetic datasets shows that the proposed FDI and FE methods offer interpretable and reasonably accurate results. However, challenges remain when applied to physics-based data, particularly due to nonlinear effects, variable initial conditions, and numerical sensitivity.

Keywords— Fault Detection and Isolation (FDI), Fault Estimation (FE), Piezo Self-sensing, Inkjet Printing, Frequency Domain, Model-based Diagnosis, Nozzle Failure.

Contents

List of Tables V

List of Figures VI

List of Symbols IX

1 Introduction 1

2 Problem Statement 5

2.1 Ink Channel Dynamics and Faults 5

2.2 Motivation, Challenges, and Objectives 7

2.3 Physics Based Model 9

3 PART I – Fault Detection and Isolation (FDI) 12

3.1 Literature Review and Existing Solutions 12

3.2 Proposed Solution 16

3.3 Methodology and Results 17

3.3.1 Comparison of Raw and Residual Data for Classification . . . 18

3.4 Performance Analysis 20

3.4.1 Improving Classification via Filter and Frequency Analysis . . 21

3.4.2 Per-Class Analysis: Raw vs. Residual Datasets 24

3.4.3 Impact of Frequency on Classification Performance 26

3.4.4 Summary 27

3.5 Simulation and Experimental Results 28

3.6 Summary and Conclusion 29

4 PART II – Fault Estimation (FE) 32

4.1 Transition from FDI to Fault Estimation (FE) 32

4.2 Literature Review and Existing Solutions 33

4.3 Proposed Solution 35

4.3.1 Problem Formulation 35

4.3.2 Observability & Validation of Identified Linear Model 37

4.3.3 Design of the Unknown Input Observer (UIO) 39

4.3.4 Modeling Considerations and Estimation Framework 42

4.4 Results on Synthetic Data 47

4.4.1 Description of the Synthetic Dataset 47

4.4.2 Fault Estimation using the DT Approach 48

4.4.3 Fault Estimation using the CT Approach 49

4.5 Evaluation on Physics-Based Model Data 51

4.6 Summary and Conclusion 53

5 Summary of Key Contributions 55

6 Conclusions and Future Work 56

Appendix 59

A Overview of Fault Classes Used in the Experiments 59

B Confusion Matrices for Simulation Dataset Classification 60

C Confusion Matrices for Real-World Dataset Classification 64

D Frequency Spectrum Analysis of Fault Classes 66

D.1 Empty Channel 1 66

D.2 Mature Air Bubble 67

D.3 Fully Blocked Nozzle 68

E Taylor Series Expansion for Discretization **69**

F Calculation of Fault Parameter f_m **71**

List of Tables

1 Symbol definitions and descriptions of physical model of CPP printers IX

2 FD and FI classification accuracy using simulation data 19

3 Mean frequency per fault class 22

4 FI accuracy comparison for raw and residual datasets 24

5 Class-wise accuracy comparison between raw and modified residual data 25

6 FD and FI accuracy on simulation dataset with raw signals and modified residual signals 28

7 FD and FI accuracy on real-world dataset with raw signals and modified residual signals 29

8 Summary of the three datasets used in this thesis. 37

9 List of fault classes for fault isolation experiments 59

10 Performance metrics per fault class for raw dataset using Random Forest classifier 62

11 Dominant frequencies for Empty Channel 1 fault class 66

12 Dominant frequencies for Mature Air Bubble fault class 67

13 Dominant frequencies for Fully Blocked Nozzle fault class 68

List of Figures

1	Printer structure and ink channel components	5
2	Schematic of sequential sensor-actuator behavior	8
3	Ink channel structure and model parameters	10
4	Current FDI filter configuration	14
5	Current fault detection process overview	15
6	Current schematic of FI filter design	15
7	Data processing pipeline for FDI experiments	17
8	Time-domain plot of a random raw signal	21
9	FFT spectrum of the raw signal	21
10	Confusion matrix for raw dataset using KNN	22
11	Confusion matrix for residual dataset using KNN	22
12	Confusion matrix for residual-based dataset using KNN	23
13	Confusion matrix for modified residual-based dataset using KNN	23
14	Bode plot of original residual filter	24
15	Bode plot of modified residual filter	24
16	Complete FDI to FE framework overview	33
17	Block diagram of diagnosis filter.	35
18	Comparison of the Frequency–Damping relationship	38
19	Block diagram comparison between a standard observer and an UIO.	39
20	State estimation results with UIO	42
21	Block diagram of the proposed fault estimation architecture.	43
22	Block diagram of discrete-time fault estimation	46
23	Block diagram of continuous-time fault estimation	47
24	Discrete-time fault estimation for a single signal using synthetic dataset	49

25 Discrete-time fault estimation accuracy across fault levels using synthetic dataset . . . 49
26 Continuous-time fault estimation for a single signal using synthetic dataset . . . 50
27 Continuous-time fault estimation accuracy across fault levels using synthetic dataset . . . 50
28 Comparison of healthy and slightly dried faulty output . . . 52
29 Discrete-time estimation for slightly dried faulty signal using physics-based dataset . . . 52
30 Comparison of healthy and Intermediately dried faulty output . . . 52
31 Discrete-time estimation for intermediately dried faulty signal using physics-based dataset . . . 52
32 Comparison of healthy and Intermediately dried faulty output . . . 52
33 Continuous-time estimation for intermediately dried faulty signal using physics-based dataset . . . 52
34 FD confusion matrices for raw and residual datasets . . . 60
35 FI confusion matrices for raw and residual datasets . . . 61
36 Confusion matrices for FD using real-world data. . . . 64
37 Confusion matrices for FI using real-world data. . . . 65
38 FFT spectrum of raw dataset for Empty Channel 1 fault class . . . 66
39 FFT spectrum of modified residual dataset for Empty Channel 1 fault class . . . 66
40 FFT spectrum of raw dataset for Mature Air Bubble fault class . . . 67
41 FFT spectrum of modified residual dataset for Mature Air Bubble fault class . . . 67
42 FFT spectrum of raw dataset for Fully Blocked Nozzle fault class . . . 68

43 FFT spectrum of modified residual dataset for Fully Blocked Nozzle fault class 68

List of Symbols

This section provides a comprehensive list of the mathematical symbols and notations used throughout this thesis. Each symbol is accompanied by a brief description of its meaning or role in the context of the analysis.

Symbol	**Description / formulation**
$V_r,\ V_n$	Volume of the restrictor and nozzle, respectively.
$\dot{V}_r,\ \dot{V}_n$	Flow rate through the restrictor and nozzle.
$\ddot{V}_r,\ \ddot{V}_n$	Rate of change of flow rate (i.e., fluid acceleration) in the restrictor and nozzle.
u	Input voltage applied to the actuator.
b	Actuator constant representing voltage-to-flow influence.
ρ	Density of the ink.
μ	Dynamic viscosity of the ink.
$L_r,\ L_n$	Lengths of the restrictor and nozzle.
$A_r,\ A_n$	Cross-sectional areas of the restrictor and nozzle.
V_{ch}	Volume of the ink channel.
c	Speed of sound in the ink.
B_{act}	Compliance of the actuator (often given by manufacturer).
$I_r,\ I_n$	Inertance of the restrictor and nozzle; represents resistance to changes in flow due to fluid inertia. Which can be approximated as: $$I_r = \frac{\rho L_r}{A_r}, \quad I_n = \frac{\rho L_n}{A_n},$$
$R_r,\ R_n$	Fluidic resistance of the restrictor and nozzle, based on fluid viscosity and geometry. Which can be approximated as: $$R_r = \frac{8\mu L_r}{\pi r_n^4}, \quad R_n = \frac{8\mu L_n}{\pi r_n^4}$$
B_t	Total compliance of the system (actuator + compressible ink volume). Which can be approximated as: $$B_t = B_{\text{act}} + \frac{V_{ch}}{\rho c^2}$$

Table 1: Symbol definitions and descriptions of physical model of CPP printers

1 Introduction

Fault diagnosis plays a critical role in ensuring the reliability and safety of modern engineering systems, particularly as equipment becomes increasingly complex and industries demand higher levels of operational dependability. Early diagnosis of faults is crucial to minimize downtime, reduce maintenance costs, and prevent catastrophic failures. This importance is particularly evident in control and systems engineering, where faults in sensors, actuators, or processes can significantly degrade system performance or compromise safety.

The combination of model-based and data-driven fault diagnosis methods has emerged as an effective approach for identifying root causes, facilitating predictive maintenance, and extending the operational life of critical assets. High-end industrial printers developed by Canon Production Printing (CPP) face challenges in detecting and isolating nozzle failures in ink channels, a crucial factor in maintaining print quality and operational efficiency.

CPP, a subsidiary of Canon located in Venlo, The Netherlands, specializes in advanced industrial printing systems [1]. As part of the NWO Digital Twin program [2], this thesis explores a hybrid fault diagnosis framework that integrates data-driven techniques with physical models. The objective is to support proactive and automated health management in high-precision printers.

CPP employs high-precision inkjet technology in its printers to ensure exceptional print quality and accuracy. More broadly, high-precision inkjet technology enables the deposition of materials such as inks, polymers, and biomaterials with remarkable precision at the micron or nanometer scale [3]. This capability allows for uniform deposition, consistent layer thickness, and precise placement of materials [3].

Beyond printing, high-precision inkjet technology is applied in various fields, including electronics, medicine, and bioprinting. Examples include thermal inkjet technology used in personalized medicine [4], nanostructured thin films and inkjet-printed micro-electrodes for sensing applications [5], and complex 3D biological structures in tissue engineering [6].

Despite these advancements, fault detection and quality assurance in printing systems remain a challenge. Traditional approaches, such as visual inspection and test charts, are still widely used. Although effective to some extent, these methods often delay fault detection and contribute to material waste.

Such inefficiencies arise from the time-consuming process of analyzing printed test patterns and physical limitations, such as the need to position a scanner module downstream of the printheads to detect errors after printing [7, 8].

These delays increase material waste in two ways: test charts consume ink and media without contributing to the final product, and late fault detection leads to accumulation of defective prints, which must be reprinted.

Piezoelectric actuators play a critical role in modern drop-on-demand (DoD) inkjet printing systems. When equipped with the appropriate sensing circuitry, these actuators can be used not only for actuation but also as self-sensing elements, allowing real-time monitoring of the jetting process and early detection of nozzle faults [9].

Techniques such as Piezo Actuator leverage this self-sensing capability to identify failures such as air bubble entrapment, electrical faults, or nozzle blockages, without relying on external imaging systems. This allows for faster fault detection and compensation, helping to maintain image quality and reduce downtime. However, challenges remain in interpreting self-sensing signals and linking signal anomalies to the physical causes of faults. These challenges motivate the development of more intelligent and robust fault detection methods for next-generation printing systems.

Beyond printing, piezoelectric self-sensing has been applied in various domains for structural health monitoring and fault detection. Examples include detecting avian influenza viruses [10], assessing concrete beam conditions [11], monitoring aerospace structures [12], and identifying damage in 3D textile composites [13]. In many of these systems, piezo signals are converted into the frequency domain to extract diagnostic parameters using threshold-based methods or advanced neural networks.

Piezoelectric self-sensing devices are also widely used in wearable electronics to monitor health by tracking heartbeat, blood pressure, and muscle activity, helping with fitness and medical diagnosis [14, 15]. They support environmental monitoring by detecting air and water pollutants, especially in remote or harsh environments, without requiring external power [15]. Vibration-based energy harvesting is increasingly used in wearable and implantable Internet of Things (IoT) devices, enabling their deployment in smart city applications [14, 15]. In robotics, these sensors enable tactile sensing and gesture recognition for human-machine interaction [14]. In medicine, they support self-powered pacemakers that generate energy from body motion while monitoring cardiac activity [15]. In civil engineering, they help monitor the structural health of bridges, roads, and dams, providing early warnings of stress or damage [15].

In current CPP systems, fault detection primarily relies on threshold-based classification using data signals [16]. Although effective, these methods do not fully capture the underlying physical changes associated with faults. To address this, [17] propose integrating physical system models with piezo self-sensing signals. This hybrid approach aims to improve the accuracy and robustness of fault detection and classification in printer nozzles.

The current method [17] relies on manual energy-based thresholds and linear regression for fault diagnosis. This thesis builds on that work by analyzing piezo signals in the frequency domain to extract fault-relevant features within specific frequency bands. These features are then integrated into a hybrid classification framework. In this approach, manual thresholding is systematically replaced by adaptive algorithmic methods, with the goal of improving the precision of fault diagnosis and addressing limitations in earlier methods.

Based on these developments, this thesis addresses the following research question.

How can the performance of fault diagnosis in high-end industrial printers be improved by analyzing piezo self-sensing datasets using a hybrid model in the frequency domain?

This research extends current work on fault detection and isolation [17] toward fault estimation. The overall aim is to enhance system reliability and support real-time applications.

This report is organized as follows: Chapter 2 introduces the CPP printing system and defines the research problem, including a detailed overview of ink channel dynamics, common fault types, and the motivation for this study. A physics-based system model is presented to support the problem formulation.

Chapter 3 (Part I) focuses on Fault Detection and Isolation (FDI). It begins with a review of relevant literature and industrial practices, followed by the proposed FDI methodology, frequency-domain feature evaluation, performance analysis, and both simulation and experimental results. The chapter is followed by a transition chapter 4.1 that introduces the shift from fault detection to fault estimation.

Chapter 4 (Part II) addresses Fault Estimation (FE). It presents a literature review, describes current methods, and introduces the proposed estimation technique, which is evaluated using simulation and experimental data.

Chapter 5 summarizes key contributions from both parts of the study, while Chapter 6 presents the final conclusions and discusses the broader implications of this research. Future work directions are also outlined. Supplementary results and extended metrics are included in Appendices.

2 Problem Statement

Canon Production Printing printers, such as the varioPRESS iV7 series, are equipped with advanced components designed for industrial-scale precision and efficiency. Key parts include the print belt, ink supply system, and printheads. Each printhead contains thousands of ink channels, allowing high-quality and detailed output for professional applications. These ink channels, shown in Figure 1, are the fundamental units of the printing process and are crucial for consistent performance and reliability [18, 19]. They are the primary focus of this study and are hereafter referred to as the *system*.

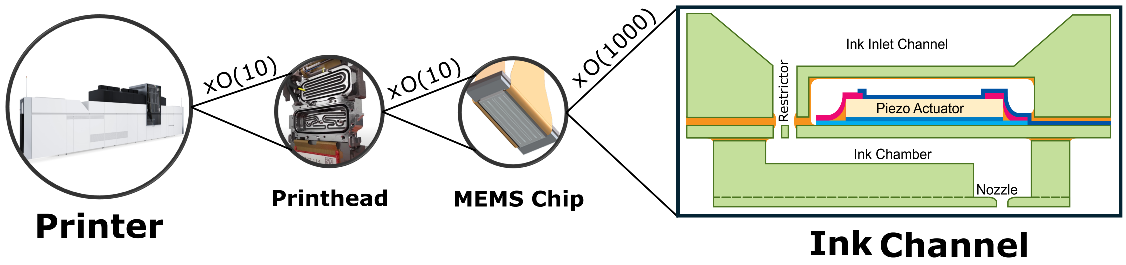

Figure 1: The printer is broken down into parts, with each part being smaller and located within the one to its left. The ink channel, which is the smallest part, is further divided into subcomponents, whose names are provided. The sequence indicates approximately how many of each subsequent component are contained within the preceding one. One printer contains hundreds of thousands of nozzles, each of which must be evaluated multiple times per second, highlighting the massive scale and complexity of the data involved [18, 19].

2.1 Ink Channel Dynamics and Faults

Each ink channel is connected to an Ink Inlet Channel that supplies ink. Ink flows from the Ink Inlet Channel through a restrictor and into the ink chamber. A piezo-electric actuator, controlled by the printhead electronics, then moves the ink from the chamber through the nozzle. When an electrical charge is applied to the actuator, it deforms, changing the volume of the ink chamber. This mechanical deformation generates a controlled pressure wave that expels a droplet [20].

Following actuation, residual mechanical oscillations remain in the ink chamber. In turn, these left over oscillations after exciting the ink in the chamber, deform the piezo actuator, generating a small current that can be monitored to assess the health of the system. In this study, the resulting electrical signal is referred to as the *self-sensing signal*, which provides valuable insight into the internal dynamics of the ink channel. By monitoring these signals, it is possible to evaluate the health of the jetting process and detect common faults such as air bubble entrapment or nozzle blockage.

The printing process is highly precise, with droplet placement resolutions reaching up to 1200 dots per inch (DPI), corresponding to a spacing of approximately $21\mu m$ between droplets. After actuation, the piezoelectric actuator functions as a sensor by measuring the flow conditions in the ink chamber. These measurements generate self-sensing signals that are essential for monitoring the performance and reliability of the system.

Although ink channels are engineered for high precision and reliability, they remain susceptible to certain faults. These include:

- **Electrical faults:** such as short circuits, open circuits, or poor electrical contacts within the piezo actuator or sensing components.
- **Nozzle faults:** for instance, air bubbles, dirt particles, or dried ink can cause partial or complete blockages [21]. Dirt particles may become trapped in the ink chamber, creating air bubbles in the nozzle. A partially dried ink layer on the nozzle plate can also lead to air entrapment [22].

These faults degrade print quality, resulting in visible defects such as ink splashes or unprinted areas (white lines) [23]. Nozzle-related faults are not only the most common but also the most relevant from both control and maintenance perspectives. In contrast to electrical faults, which are often permanent, nozzle faults are typically repairable.

As a result, this research focuses on nozzle faults, as they represent a category of failures where diagnostic insights can enable meaningful corrective actions. A detailed classification of the faults considered in this study is provided in Appendix A.

An effective fault diagnosis is essential to maintain high print quality, reduce waste, and control operational costs. Additionally, consistent output enhances user satisfaction and contributes to the competitiveness of the technology. Early detection, isolation, and estimation of faults enable the system to compensate for failed nozzles and maintain stable performance.

2.2 Motivation, Challenges, and Objectives

CPP's industrial printing systems operate at an exceptional scale and speed, with hundreds of thousands of nozzles evaluated at microsecond intervals. This operational complexity presents a diagnostic challenge, particularly in detecting and responding to faults with sufficient accuracy.

One of the most promising opportunities lies in the use of piezoelectric actuators as self-sensing elements. These actuators, which already serve as the system's means of droplet ejection, also produce measurable electrical signals during their recovery phase. These self-sensing signals reflect the internal dynamics of the ink channel and can, in principle, support real-time monitoring without the need for additional hardware. However, interpreting these signals in a generalizable and robust way, especially under realistic operating conditions, remains a significant challenge.

At the same time, practical incentives drive the need for improved diagnostics. The most common faults are those affecting the nozzles, which are typically not permanent and can often be resolved through compensation or cleaning. Unlike electrical faults, nozzle faults are generally recoverable if detected early. This creates a strong case for developing diagnostic systems capable of identifying such faults in real time.

Existing methods for fault detection primarily rely on external inspection tools such as test charts or downstream scanners. These techniques are not only time-consuming but also reactive in nature; faults are detected only after they have affected the printed output. Moreover, the inspection process itself consumes material and introduces waste. These inefficiencies further highlight the potential benefit of a model-informed, signal-based diagnostic approach that can anticipate faults before visible defects occur.

To address these issues, this thesis aims to develop a comprehensive diagnostic framework that performs fault detection, isolation, and estimation (FDI+E) for CPP systems using piezoelectric self-sensing signals. The research is guided by the following objectives:

- **Fault detection:** Identify whether a given measurement corresponds to a healthy or faulty state (binary classification).
- **Fault isolation:** Determine the type of fault present once a faulty condition is detected (multi-class classification).
- **Fault estimation:** Track the evolution of the fault over time and assess its severity.

Achieving these objectives presents several technical challenges:

- **Small Time and Space Scales:** The system operates on microsecond time scales and micrometer spatial dimensions, complicating both data acquisition and real-time analysis [24].
- **Same Sensor and actuator:** The piezoelectric element serves as both the actuator and the sensor. As illustrated in the plot below, during the actuation phase, an input signal is applied to the system; however, the output signal cannot be acquired at that moment due to the element's dual function. After this, there is a short delay, and then the actuator switches to sensing mode. At that point, it can detect and record the system's response. This sequential operation prevents simultaneous access to input and output data, which introduces limitations and increases the complexity of system identification.

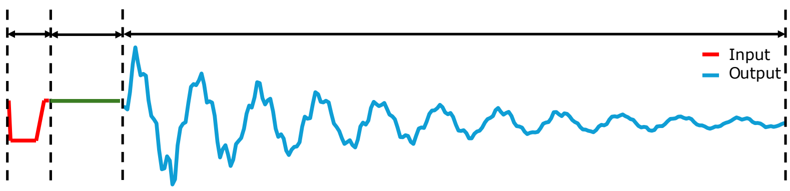

Figure 2: Schematic illustration of the sequential operation of the piezoelectric element, which alternates between actuation and sensing. The plot conceptually outlines three distinct phases: actuation, a brief transition delay, and sensing. This figure is intended for illustrative purposes and does not depict measured data.

- **Absence of a System Model:** No system model is available at the start. The system must be modeled directly from data as part of the diagnostic process.

Despite these challenges, this research benefits from access to a large set of simulated data, labeled according to known fault classes. Such data enables the development and validation of supervised learning methods under controlled conditions. In contrast to real-world scenarios, where the cause of a fault is often identified only after the fault has occurred, simulation provides ground truth that facilitates the extraction of discriminative features and the evaluation of classification performance.

Once the proposed methods demonstrate sufficient accuracy on simulated data, they are applied to real-world measurements. In selected cases where the presence of specific faults is known with high confidence, performance is evaluated to assess generalizability. Demonstrating consistent behavior across both domains builds confidence in the method's robustness and supports its potential for use in production environments.

2.3 Physics Based Model

As discussed previously, one of the key challenges in fault diagnosis for CPP printers is the absence of an established physical model for the ink channel. To address this limitation, a simplified model of the ink channel dynamics is constructed as a foundation for the proposed hybrid diagnostic framework.

This study builds on prior modeling efforts, particularly the work in [17], which provides a baseline mathematical representation of the ink channel behavior. The model captures the dynamics of ink flow within the system, driven by a piezoelectric actuator and constrained by the geometry and material properties of internal components.

The governing differential equations are shown below. These describe the relationship between ink volume changes and input voltage, taking into account inertial, resistive, and compressibility effects within the restrictor and nozzle regions.

$$
\begin{aligned}
I_n \ddot{V}_n + I_r \ddot{V}_r &= -\frac{2(V_r + V_n - bu)}{B_t} - R_r \dot{V}_r - R_n \dot{V}_n \\
I_n \ddot{V}_n + R_n \dot{V}_n &= I_r \ddot{V}_r + R_r \dot{V}_r
\end{aligned}
\tag{1}
$$

A schematic of the ink channel structure is presented in Figure 3, illustrating the key components, namely, the restrictor, ink chamber, piezo actuator, and nozzle. The variables used in the equations correspond directly to these physical elements.

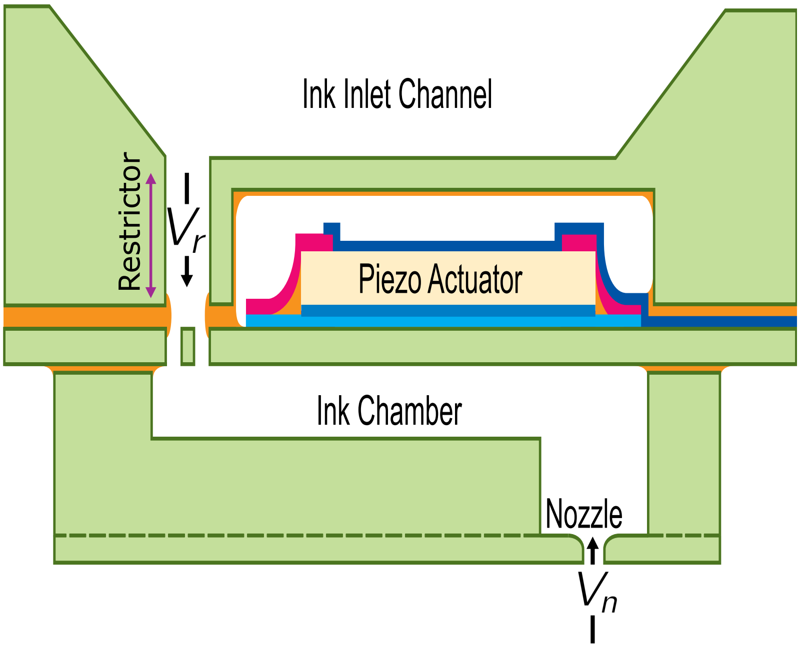

Figure 3: Schematic of the ink channel system, highlighting key physical components and their correspondence to the parameters used in the dynamic model.

In these equations, V_r and V_n denote the fluid volumes at the restrictor and nozzle, respectively. The first and second derivatives of these volumes with respect to time represent flow rate and flow acceleration. The parameters I_r and I_n capture the inertial properties of the fluid, while R_r and R_n represent resistive effects due to fluid viscosity and channel geometry. These parameters are derived from standard fluid mechanics formulations.

The system's compliance is modeled by combining the compressibility of the ink and the flexibility of the actuator (B_{act}) into a single term, B_t. The input signal, u, represents the voltage applied to the actuator, and its contribution to the chamber volume change is scaled by the constant b. A complete list of model parameters, along with their physical interpretations and approximate expressions, is provided in Table 1.

Based on (1) the dynamic behavior of the system can be represented in state-space form, with the corresponding state-space matrices defined as follows:

To support simulation, analysis, and control design, the differential equations (1) are converted into a state-space form. The resulting system of first-order equations is expressed as:

$$
\begin{aligned}
\underbrace{\begin{bmatrix} \dot{V}_r \\ \dot{V}_n \\ \ddot{V}_r \\ \ddot{V}_n \end{bmatrix}}_{\dot{x}} &= \underbrace{\begin{bmatrix} 0 & 0 & 1 & 0 \\ 0 & 0 & 0 & 1 \\ \frac{1}{I_r B_t} & -\frac{1}{I_r B_t} & -\frac{R_r}{I_r} & 0 \\ -\frac{1}{I_n B_t} & \frac{1}{I_n B_t} & 0 & -\frac{R_n}{I_n} \end{bmatrix}}_{A} \underbrace{\begin{bmatrix} V_r \\ V_n \\ \dot{V}_r \\ \dot{V}_n \end{bmatrix}}_{x} + \underbrace{\begin{bmatrix} 0 \\ 0 \\ \frac{b}{I_r B_t} \\ \frac{b}{I_n B_t} \end{bmatrix}}_{B_u} u, \\
y &= \underbrace{\begin{bmatrix} 0 & 0 & c & c \end{bmatrix}}_{C} \underbrace{\begin{bmatrix} V_r \\ V_n \\ \dot{V}_r \\ \dot{V}_n \end{bmatrix}}_{x}
\end{aligned}
\tag{2}
$$

This state-space model provides a compact and analytically tractable representation of the system dynamics. It forms the basis for designing model-based filters and generating residuals used for fault diagnosis. The following chapters build on this model to develop and evaluate the proposed diagnostic framework.

3 PART I – Fault Detection and Isolation (FDI)

This part of the thesis presents the design, implementation, and evaluation of a FDI framework for piezo-based industrial printing systems. The aim is to develop a reliable and interpretable method that can identify and distinguish between different types of faults using piezo self-sensing signals. This section includes a review of existing methods, a proposed hybrid approach, methodological details, performance analysis, and experimental validation.

3.1 Literature Review and Existing Solutions

Several methods have been proposed for fault diagnosis in high-end industrial printing systems. Traditionally, quality assurance has relied on visual inspection techniques using dedicated test charts. Although widely adopted in practice, these approaches introduce significant delays in detecting faults and often lead to increased material waste. The delay arises for two main reasons: (1) analyzing printed test patterns is time-consuming, and (2) scanner modules are physically located downstream of the printheads, introducing latency between fault occurrence and detection [7, 8].

Test charts also consume ink and media without contributing to the final printed product. Moreover, delayed detection means that more defective prints are produced before corrective action is taken. These prints must be discarded and reprinted, which increases ink, substrate, and energy consumption, ultimately affecting the overall productivity and sustainability of the printing process.

To mitigate these issues, recent work has explored signal processing-based methods that utilize piezo self-sensing signals [16]. In these methods, key performance indicators (KPIs) are typically extracted in the frequency domain, and faults are detected using threshold-based techniques.

Although this self-sensing approach enables real-time monitoring and reduces reliance on external scanners, it does not provide a complete picture of printing performance. The signals primarily capture the dynamics within the ink channel and do not reflect how the ink behaves on the substrate, which may be influenced by external factors such as airflow or material absorption. As a result, self-sensing approaches are often combined with traditional test charts to validate print quality. However, this combined solution has its own limitations:

- **Lack of a Physical System Model:** Without a dynamic model of the system, it is difficult to generalize this method in varying operating conditions or predict how faults might develop over time. This limits its applicability for more advanced diagnostic tasks such as fault estimation, areas where model-based approaches excel.
- **Sensitivity to Thresholds:** The reliance on fixed parametric thresholds makes the system sensitive to changes in operating conditions, such as temperature variations, ink properties, or aging actuators. This can result in false positives or missed detections.

Beyond these methodological limitations, CPP printers also present unique structural challenges. A particularly important one is the absence of simultaneous input-output data, which complicates system identification.

This issue stems from the dual role of the piezoelectric actuator in CPP systems, it acts both as an actuator and as a sensor. During operation, the system is excited by a short trapezoidal pulse, and only after the pulse ends does the sensor start recording the response. Because input and output are not measured simultaneously, it is difficult to apply standard identification techniques that depend on synchronized data.

To address some of these limitations, recent research by [17] proposes a hybrid approach that combines model-based and data-driven techniques for fault diagnosis. This method takes advantage of both domains: Incorporating a theoretical model of the inkjet system dynamics while simultaneously utilizing real-time self-sensing signal data. By merging these two sources of information, the method improves both the accuracy and the robustness of fault detection.The proposed filter is computationally efficient, capable of processing signals in real time, and scalable for deployment in systems where direct observation is not feasible.

Since the system lacks available input data during actuation, it is modeled as autonomous in [17], meaning that input signals are not explicitly required. However, this shifts the challenge to estimating the initial system state, which varies from measurement to measurement. To approximate the initial state, key parameters, such as amplitude, frequency, damping, and phase, are extracted from the signals. These features are then used to reconstruct the initial flow rate and volume. By averaging across multiple measurements, a noise-reduced and representative estimate of the initial state is obtained.

The piezo self-sensing signal, which is linearly related to the flow rate, enables signal analysis without converting it into physical quantities, provided the scaling remains consistent. The complete FDI pipeline is shown in Figure 4.

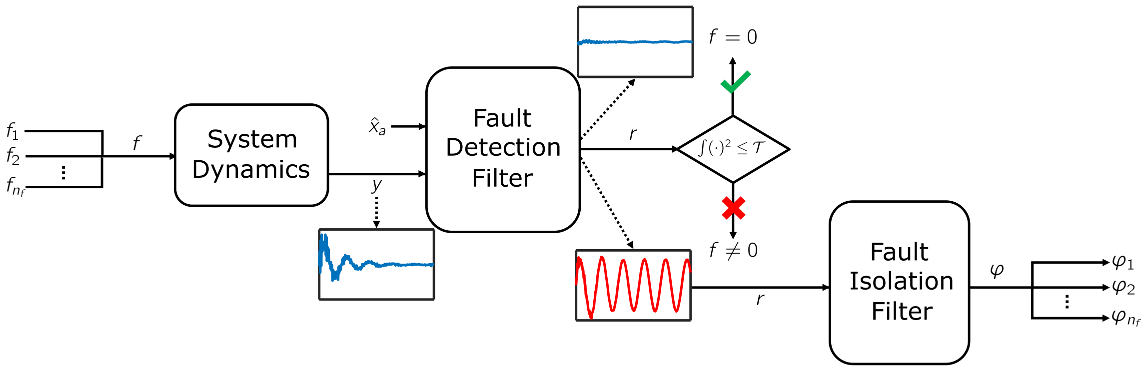

Figure 4: Overall configuration of the FDI filter, combining model-based residual generation with data-driven [17].

To establish a suitable model of the system, a grey-box system identification is performed using real measurements from CPP printers. The identified model forms the basis for constructing a residual generator, which distinguishes between healthy and faulty operation. This residual remains near zero during normal operation and deviates in response to faults. Fault detection is then carried out by applying a manually defined energy threshold to the residual signal, as illustrated in Figure 5.

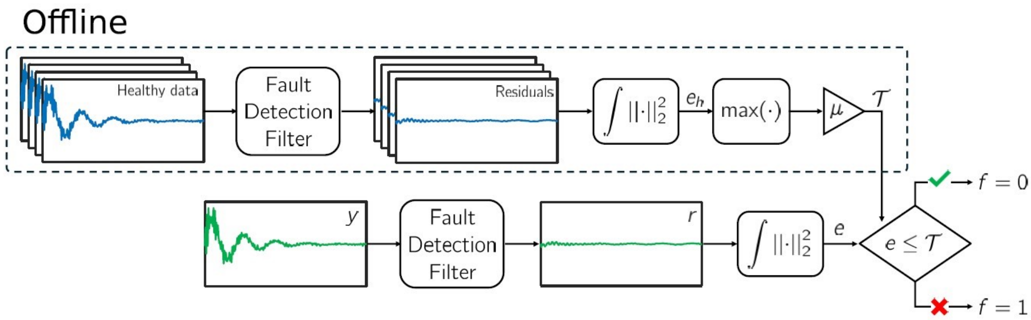

Figure 5: Fault detection process using the model-based residual signal. The offline section illustrates how the energy threshold τ is determined, which is then applied to detect faults in the output signal y [17].

The same residual is used in the regression-based fault isolation (FI) step. Here, the residual from an incoming signal is compared to a set of reference residuals associated with known fault types. A linear regression model quantifies the similarity, assigning probabilities to each candidate fault. The fault class with the highest probability is selected. This procedure is summarized in Figure 6.

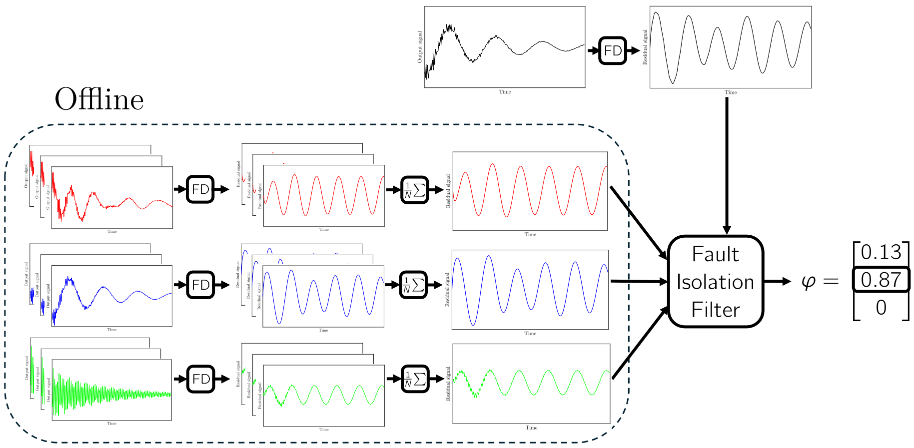

Figure 6: Schematic overview of the design and implementation of FI filter. Residual signals are compared to reference fault signatures using linear regression [17].

This hybrid framework integrates the robustness of model-based design with the adaptability of data-driven analysis. It helps address key challenges in CPP systems, such as autonomous modeling and initial state estimation. However, the method continues to face several limitations, particularly in fault isolation performance across all fault types. Its reliance on manually tuned thresholds and reference datasets restricts the system to a small number of predefined fault classes and known fault patterns. In practical applications, only a limited subset of fault types is included in the fault isolation module, and the overall accuracy varies between different fault categories.

The objective of this research is to extend the existing approach by addressing these shortcomings. Specifically, it aims to improve the generalizability and scalability of fault isolation by reducing dependence on offline fault signatures and manually defined thresholds. The goal is to support more fault types and enable FDI under a wider range of conditions. In doing so, the proposed method seeks to improve diagnostic speed and consistency while reducing reliance on prior knowledge.

3.2 Proposed Solution

This section presents a hybrid framework that integrates model-based and data-driven techniques to improve FDI in piezo-based printing systems. The proposed approach aims to address known limitations of existing methods by combining a time-domain model of the system dynamics with frequency-domain analysis of features extracted from the output signals.

This dual-domain strategy offers two main advantages. First, it eliminates the need for manually tuned, energy-based thresholds commonly used in traditional fault detection. Second, it removes the dependency on pre-computed residuals associated with specific, known fault classes.

For the classification and isolation of faults, two machine learning algorithms are used: K-Nearest Neighbors (KNN) [25] and Random Forest [26], both of which are well-established in the machine learning literature. These classifiers operate on frequency-domain features derived from the system's output signals. By avoiding fixed thresholds and pre-defined reference datasets, the method shows greater potential to generalize to previously unseen fault types, which is particularly valuable in real-time industrial applications where operating conditions may vary.

To enhance the framework's adaptability, multiple feature extraction methods are evaluated. Additionally, a comparative analysis is conducted between using raw output signals and residual signals as classifier inputs. The aim is to identify the configuration that yields the most reliable fault diagnosis performance under realistic industrial scenarios.

3.3 Methodology and Results

This section describes the methodology used to evaluate the proposed hybrid FDI approach and presents results comparing classification performance based on raw signals and model-based residuals.

Figure 7 provides an overview of the experimental process used to generate the datasets for training and evaluation. The process begins with the extraction of Key Performance Indicators (KPIs) from raw simulation data (Box 1). In total, seven KPIs are computed: DC Offset, Dominant Frequency, Damping Ratio, Amplitude, Phase, Energy, and Magnitude.

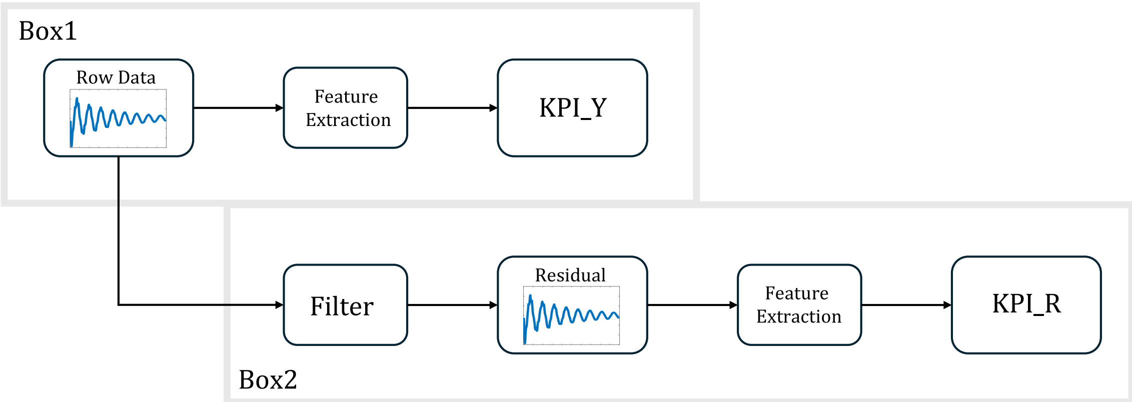

Figure 7: Overview of the data generation and processing pipeline for FDI experiments. Raw signals are processed using a feature extraction method proposed by CPP [16]. Residual filters are then applied to generate a second dataset based on residual signals. This results in two datasets: one using features from the raw signal (`KPI_Y`), and one from the residuals (`KPI_R`).

The feature extraction method used in this study is based on the approach proposed by [16], which assumes that the input signals are primarily sinusoidal. Accordingly, the method extracts features that characterize periodic behavior. It does not capture non-sinusoidal patterns such as transients, noise bursts, or other irregularities. As a result, the method is most effective when the measured signals, and by extension, the residuals, exhibit predominantly sinusoidal characteristics, which may not hold true under all real-world fault conditions.

In this context, the assumption of sinusoidal behavior is considered reasonable. According to technical input from Canon, the faults of interest in the targeted printing systems tend to produce self-sensing signals with sinusoidal structure. Additionally, the residual filters are designed with imaginary poles to promote the generation of sinusoidal residuals. Therefore, the feature extraction approach is well aligned with the nature of both the raw and residual signals observed in this application.

In the next stage of the process (Box 2), model-based filters are applied to the raw signals, and KPIs are extracted from the resulting residual trajectories. This yields two datasets: `KPI_Y`, based on features from raw signals, and `KPI_R`, based on residuals. These datasets are evaluated and compared in Section 3.3.1 to assess their effectiveness for fault classification.

3.3.1 Comparison of Raw and Residual Data for Classification

This section compares classification performance using features extracted from raw signals versus those from residual signals. Two machine learning algorithms, KNN and Random Forest, are applied to evaluate which combination of data representation and classifier yields the highest accuracy for FDI.

Table 2 summarizes the results. For the fault detection(FD) task, the dataset includes only faulty and healthy signals. The fault isolation(FI) task includes the healthy class as well. This inclusion is intentional, as the objective is to evaluate FDI in a single step. The classifier is expected to determine whether a signal is faulty and, if so, assign it to the corresponding fault class. This integrated FDI setup simplifies computation and enables faster, more efficient decision-making features that are valuable in real-time systems.

The dataset design ensures class balance and supports a fair comparison of model performance across classifiers and input representations.

Signal Type	FD Accuracy (%)		FI Accuracy (%)	
	KNN	Random Forest	KNN	Random Forest
KPI_Y	98.22	**99.32**	88.30	**94.36**
KPI_R	94.42	94.16	79.33	78.53
Dataset (Simulation)				
Number of Healthy Samples	2,500		500	
Number of Faulty Samples	2,500		250 per class	
Number of Fault Classes	10		10	
Total Samples	5,000		3,000	

Table 2: Classification accuracy for FD and FI using raw signals (KPI_Y) and residual signals (KPI_R), evaluated with KNN and Random Forest. Results are reported for simulation datasets, along with dataset structures.

As shown, both classifiers perform well, especially with features derived from raw signals. The best FD accuracy of 99.32% and FI accuracy of 94.36% are achieved using Random Forest on KPI_Y.

These results suggest that raw signals retain more relevant information than residual signals, enabling more accurate classification in both FD and FI tasks. Full confusion matrices and additional performance metrics are provided in Appendix B.

In the classification setup, faulty nozzles are defined as the positive class, while healthy nozzles are treated as negative. This aligns with typical fault detection conventions, where the presence of a fault triggers a positive prediction.

From an operational perspective, CPP prefers minimizing false negatives, even at the cost of increasing false positives. A false negative, misclassifying a faulty nozzle as healthy, can lead to undercompensation, producing a visible white line in the printed output. In contrast, a false positive results in overcompensation for a healthy nozzle, which may introduce a slightly darker line, typically less noticeable and more acceptable to end users [27].

For this reason, a conservative strategy that favors false positives helps maintain higher perceived print quality. The classifier behavior observed in this study supports this preference, with the false negative rate remaining low across most fault categories.

In particular, the Random Forest model trained on KPI_Y performs well for FD . It achieves an F1-score of 99.32% for the fault class, with low false positive and false negative rates. In FI, Most fault types are classified with accuracy above 93.00%, including *Empty Channels*, *Fully Blocked Nozzles* and *Deeply Dried Nozzle*, which are identified perfectly. A drop in F1-score is observed for subtle faults like *Partially Blocked* and *Intermediately Dried Nozzles*, though overall accuracy remains acceptable.

These findings support the use of raw signal features for nozzle fault classification and confirm that the approach offers robustness across a range of fault types.

It is important to note that, in real-world settings, fewer than 1% of all measured signals are faulty. However, because industrial systems often include tens or hundreds of thousands of nozzles, the likelihood of encountering faults during regular operation is high. For example, with 100,000 active nozzles, even a fault probability of 0.001% per nozzle leads to frequent fault occurrences at the system level. In this context, the ability to isolate these rare faults with high precision becomes highly significant, as it ensures minimal disruption and supports confident decision-making in the diagnosis of nozzle faults.

Once a faulty nozzle is identified, compensation is performed immediately by activating neighboring nozzles to cover the affected area. Although compensation is initiated regardless of the specific fault type, identifying the root cause is still valuable. It supports long-term maintenance decisions such as cleaning or nozzle deactivation when needed.

A further discussion of the residual signal dataset and its limitations follows in the next section.

3.4 Performance Analysis

This section examines the factors contributing to the lower classification performance observed when using residual-based features compared to raw signal features. By analyzing the frequency content of residual signals using Fast Fourier Transform (FFT), the goal is to assess whether relevant information is lost during residual generation and how this affects FD. Additionally, the analysis explores which fault classes benefit more from either raw signals, residuals, or both, thereby clarifying the complementary strengths of each approach.

To evaluate frequency-domain characteristics, it is essential to understand how dominant frequency features are extracted and integrated into the KPI datasets. Figures 8 and 9 present a representative raw signal and its FFT spectrum. The dominant frequency, as shown in the spectrum, is included as one of the KPIs in the dataset.

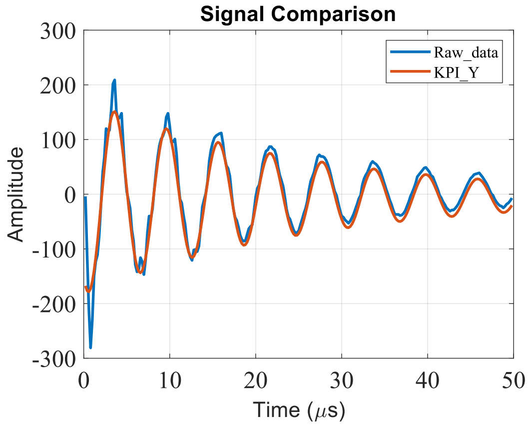

Figure 8: Time-domain plot of a randomly selected raw signal and its corresponding `KPI_Y`.

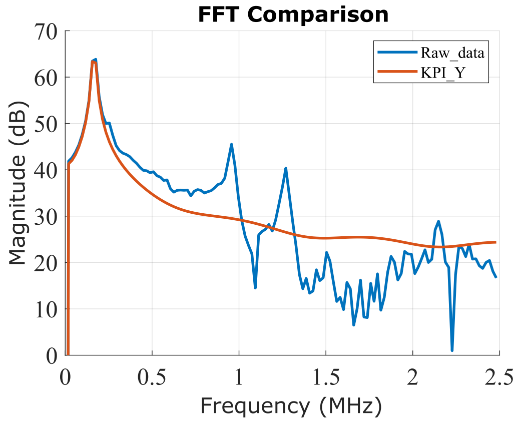

Figure 9: FFT spectrum of signals shown in Figure 8, showing the extracted dominant frequency used as a KPI.

The comparison of the raw signal and its extracted version, `KPI_Y`, shows that the reconstructed signal retains the main structure of the original. In the time domain, this similarity reflects that the signal is primarily composed of a single dominant frequency component. In the frequency domain, this becomes clearer, as most of the spectral energy is concentrated around a single peak. This confirms that the KPI extraction method, adapted from the approach in [16], focuses on dominant frequency content and assumes that signals are predominantly sinusoidal.

3.4.1 Improving Classification via Filter and Frequency Analysis

This section investigates the limitations observed in the residual-based dataset and outlines a filtering strategy aimed at enhancing classification accuracy. As illustrated in Figure 11, the confusion matrix highlights several fault classes with reduced classification performance comparing to the raw dataset (`KPI_Y`).

To understand the root cause of these misclassifications, Table 3 presents the mean dominant frequencies of each fault class. The analysis indicates that the residual generation process removes important high-frequency content for the *Empty Channel* faults, which appears to limit the classifier's ability to distinguish these classes reliably.

In contrast, for fault classes such as *Air Bubbles*, *Partially Blocked Nozzles*, and *Dried Nozzles*, the classification difficulty seems to stem from insufficiently distinctive features, rather than high-frequency loss. These classes often exhibit overlapping frequency characteristics, which remain challenging to separate even before residual processing.

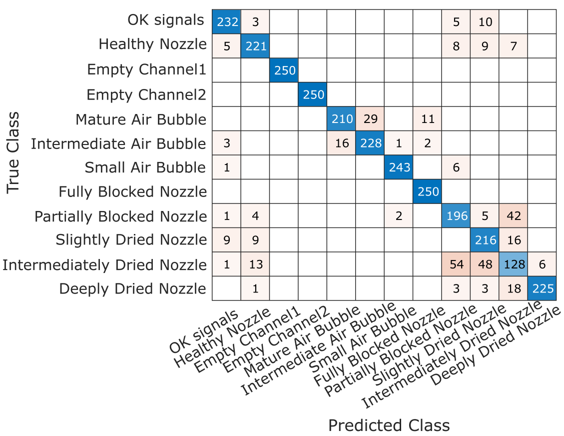

Figure 10: Confusion matrix for raw dataset (`KPI_Y`) using KNN.

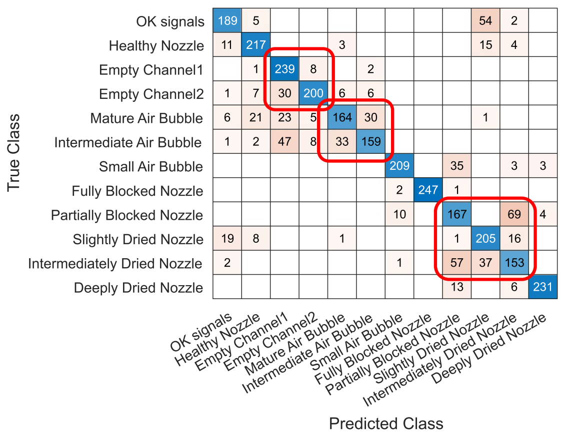

Figure 11: Confusion matrix for the residual-based dataset (`KPI_R`) using the KNN classifier. Misclassified classes are highlighted in red.

Fault Class	**Mean Frequency (KHz)**
OK signals	237.150
Healthy Nozzle	237.170
Empty Channel1	**2124.400**
Empty Channel2	**1423.400**
Mature Air Bubble	357.450
Intermediate Air Bubble	330.780
Small Air Bubble	189.720
Fully Blocked Nozzle	166.350
Partially Blocked Nozzle	200.480
Slightly Dried Nozzle	225.130
Intermediately Dried Nozzle	212.730
Deeply Dried Nozzle	189.650

Table 3: Mean frequency (in kHz) of each fault class extracted from raw signals. Fault classes with significantly higher frequencies,such as Empty Channel 1 and 2, are highlighted in bold.

The red boxes in Figure 11 highlight the fault classes where the residual-based dataset demonstrates poor classification performance. To recover critical spectral information, a modified residual filter is introduced. This new design incorporates additional imaginary poles targeted at three frequency ranges: (1) the dominant frequency of *Empty Channel 1*, (2) the average frequency of *Mature* and *Intermediate Air Bubbles*, and (3) the mean of *Partially Blocked*, *Slightly Dried*, and *Intermediately Dried Nozzles*.

However, directly adding imaginary poles introduces instability into the filter design. To mitigate this, a loop-shaping procedure is applied. The Bode plot is used to assess the stability and ensure that the modified filter maintains adequate gain and phase margins. The inclusion of proportional (K) and integral (I) terms helps achieve a stable filter configuration suitable for practical implementation.

The results of this modification are evaluated in three ways:

1. Confusion Matrices: Figure 12 shows the confusion matrix of the original residual-based dataset (`KPI_R`). Figure 13 presents the results after applying the modified filter. The improvement in classification accuracy is especially evident for previously underperforming fault classes.

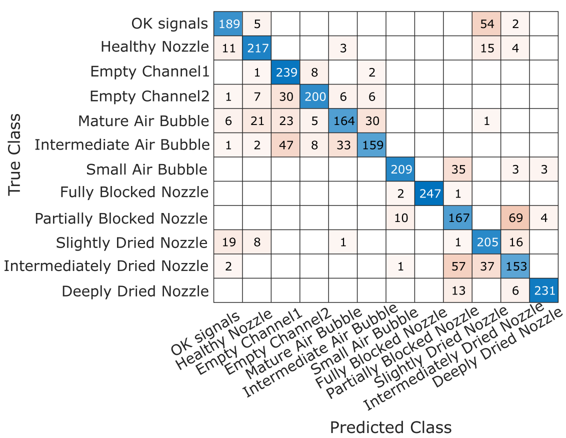

Figure 12: Original confusion matrix for residual-based dataset (`KPI_R`) using KNN.

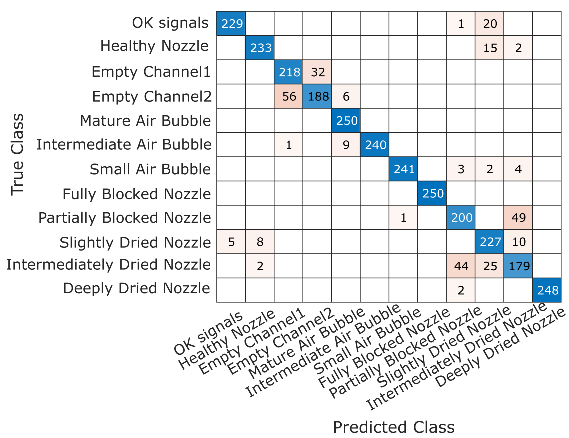

Figure 13: Confusion matrix for modified dataset (`KPI_R_Modified`) using KNN. Improved isolation is evident.

2. Bode Plots: Figures 14 and 15 show the frequency responses of the original and modified filters. The modified design introduces the desired frequency selectivity while preserving stability.

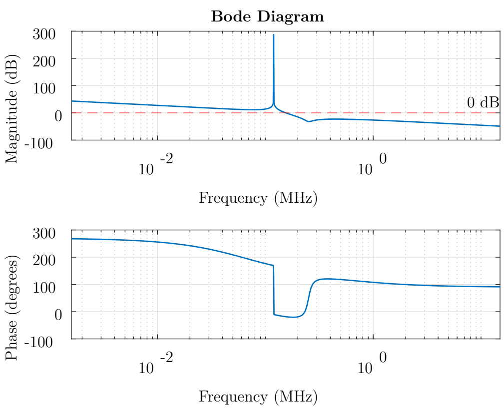

Figure 14: Bode plot of the original residual filter (KPI_R).

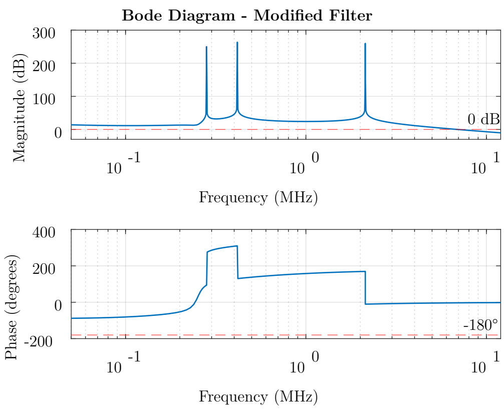

Figure 15: Bode plot of modified residual filter (KPI_R_Modified). Loop shaping ensures stability.

3. Fault Isolation Accuracy: Table 4 summarizes the improvement in classification performance for both KNN and Random Forest classifiers. The modified residual dataset (KPI_R_Modified) achieves a notable increase in fault isolation accuracy, approaching the performance of the raw dataset (KPI_Y).

Dataset	FI Accuracy (%)	
	kNN	Random Forest
KPI_Y	88.30	94.36
KPI_R	79.33	78.53
KPI_R_Modified	90.10	91.23

Table 4: Comparison of fault isolation accuracy for raw data (KPI_Y), original residual based dataset (KPI_R), and modified residual based dataset (KPI_R_Modified).

These results demonstrate that targeted filter modifications can improve the classification accuracy. The revised design brings residual-based classification closer to the performance achieved with raw signal features, while preserving the benefits of model-based residual generation.

3.4.2 Per-Class Analysis: Raw vs. Residual Datasets

This section compares the per-class classification performance of the raw dataset (KPI_Y) and the modified residual-based dataset (KPI_R_Modified) using KKN classifier. The confusion matrix for the raw data appears in Figure 35 (Appendix), while the corresponding matrix for the residual dataset is shown in Figure 13. The analysis focuses on the diagonal elements of each matrix, which represent the percentage of correctly classified samples for each fault class. A summary is presented in Table 5.

Class	CM (Correct) (%)		Better Classification
	Raw Data	Residual	
OK signals	92.80	91.60	`KPI_Y`
Healthy Nozzle	88.40	93.20	`KPI_R`
Empty Channel 1	**100.0**	87.20	`KPI_Y`
Empty Channel 2	**100.0**	75.20	`KPI_Y`
Mature Air Bubble	84.00	**100.0**	`KPI_R`
Intermediate Air Bubble	91.20	96.00	`KPI_R`
Small Air Bubble	97.20	96.40	`KPI_Y`
Fully Blocked Nozzle	**100.0**	**100.0**	**The same**
Partially Blocked Nozzle	78.40	80.00	`KPI_R`
Slightly Dried Nozzle	86.40	90.80	`KPI_R`
Intermediately Dried Nozzle	51.20	71.60	`KPI_R`
Deeply Dried Nozzle	90.00	99.20	`KPI_R`

Table 5: Per-class comparison of classification accuracy for raw data (`KPI_Y`) and modified residual data (`KPI_R_Modified`) using KNN. Highlighted rows indicate major focus of this section.

Several observations emerge from Table 5:

- **Empty Channel 1 and 2** are better classified using raw data, which suggests that important distinguishing components are not preserved in the residual signal.
- **Mature Air Bubble** and other classes show improved performance with residual-based features, likely due to the updated filter structure that better captures their frequency characteristics.
- **Fully Blocked Nozzle** achieves identical performance in both datasets, indicating its features are well preserved regardless of the representation.

These results highlight the trade-offs involved in using residual generation for fault classification. Although the residual filter improves performance for several fault types, it also introduces limitations for others by filtering out useful frequency content. The next section investigates these effects in more detail through spectral analysis of selected classes.

3.4.3 Impact of Frequency on Classification Performance

As illustrated in Figure 11, the residual-based dataset shows limited classification performance for certain fault classes, particularly those highlighted in red. To investigate this relationship more closely, three representative fault types and their corresponding mean frequencies are selected for further analysis: *Empty Channel 1* (2124.4 kHz), *Mature Air Bubble* (357.5 kHz), and *Fully Blocked Nozzle* (166.4 kHz). These cases reflect distinct classification patterns and help explore how frequency content influences model performance.

The spectral analysis reveals different behaviors across these faults when comparing raw and residual signals. For the *Empty Channel 1* fault, the raw signal exhibits dominant peaks around 2031 kHz and 2246 kHz, closely surrounding the expected mean. In contrast, the residual signal shows a dominant peak at approximately 215 kHz, suggesting that significant high-frequency content is lost during residual generation. This frequency shift likely contributes to the reduced classification accuracy observed for this class in the residual-based dataset.

For the *Mature Air Bubble* fault, the residual signal retains a dominant frequency around 215 kHz, which remains reasonably close to the expected 357 kHz. Meanwhile, the raw signal spans a broader frequency range (roughly 293–410 kHz), which may dilute class-specific features. In this case, the more focused spectral content of the residual signal appears to support improved classification.

In the case of the *Fully Blocked Nozzle* fault, both datasets show dominant peaks near the expected fault frequency, 176 kHz in the raw data and 215 kHz in the residuals. As a result, both representations yield similar classification performance.

Overall, these findings illustrate how the preservation or distortion of fault-specific frequency components directly influences the classification success of different faults. Additional spectra and figures supporting these observations are provided in Appendix D.

3.4.4 Summary

This analysis shows that classification performance in fault diagnosis closely depends on the spectral properties of the input signals and the design of the residual filter. By modifying the filter to better preserve relevant frequency components, the classification accuracy of the residual-based dataset improves, especially for fault classes previously misclassified. The per-class comparison confirms that raw signals tend to perform better for faults characterized by high-frequency content, while residual signals are more effective for identifying faults with dominant low-frequency behavior.

Although the raw dataset requires less computational effort and avoids the need for filter design, the residual-based approach offers advantages in specific cases. As indicated in Table 5, more fault classes benefit from residual-based classification than from raw data, despite the additional complexity involved.

This indicates that the choice between raw and residual datasets should not be based solely on computational cost, but must critically consider the frequency content of the fault signals. Residuals are particularly effective at enhancing fault detectability for low-frequency faults by suppressing irrelevant dynamics and disturbances, aligning with principles outlined in recent model-based diagnosis research [28, 29].

For faults that involve higher-frequency features, however, raw signals often preserve key information more effectively, as filtering may attenuate important components. In such cases, raw signal-based classification may offer more reliable results.

Overall, this section emphasizes the value of frequency-aware feature extraction and filter design. Understanding the spectral characteristics of fault signals is essential for selecting an appropriate strategy, whether residual-based or raw-data-based, to improve fault isolation under varying conditions.

3.5 Simulation and Experimental Results

After addressing the missing frequency components in the residual-based dataset, the proposed FD and fault FI framework is evaluated on both simulated and real-world datasets.

As discussed earlier, the real-world dataset contains only a limited number of labeled fault classes. This limitation mainly arises from practical challenges in accurately labeling real data. In many cases, the exact fault type is not known at the time of occurrence and can only be inferred retrospectively, introducing some degree of uncertainty into the ground truth.

To support reliable validation, this study uses simulated datasets with known ground truth. These datasets cover a broader range of fault types and enable a controlled evaluation of the classification framework. In contrast, the real-world dataset primarily contains *drying* faults, as these are easier to reproduce experimentally and to interpret in the context of fault estimation. Due to the limited size of the real-world dataset,80% is allocated for training and the remaining 20% for testing.

Tables 6 and 7 summarize the classification accuracy for simulated and real datasets respectively. They compare the performance of raw signals (`KPI_Y`) and modified residual signals (`KPI_R_Modified`) using two classifiers: KNN and Random Forest. All results presented are based on the test set.

Signal Type	**FD Accuracy (%)**		**FI Accuracy (%)**	
	KNN	**Random Forest**	**KNN**	**Random Forest**
`KPI_Y`	98.22	99.32	88.30	94.36
`KPI_R_Modified`	98.68	98.74	90.10	91.23

Dataset

Number of Healthy Samples	2,500	500
Number of Faulty Samples	2,500	250 per class
Number of Fault Classes	10	10
Total Samples	5,000	3,000

Table 6: FD and FI accuracies on the **simulation dataset** using raw signals (`KPI_Y`) and modified residual signals (`KPI_R_Modified`), evaluated with KNN and Random Forest classifiers. Dataset statistics are included below.

Signal Type	FD Accuracy (%)		FI Accuracy (%)	
	KNN	Random Forest	KNN	Random Forest
KPI_Y	98.33	100.00	91.11	93.33
KPI_R_Modified	98.33	98.33	93.33	93.33
Dataset				
Number of Healthy Samples	100		100	
Number of Faulty Samples	200		100 per class	
Number of Fault Classes	2		2	
Total Samples	300		300	
Train/Test Split	80% / 20%		80% / 20%	

Table 7: FD and FI accuracies on the **real-world dataset** using raw signals (`KPI_Y_Real`) and modified residual signals (`KPI_R_Modified_Real`), evaluated with KNN and Random Forest classifiers. Dataset statistics are summarized below.

The results show that the proposed method performs reliably across both datasets. High FD and FI accuracies are achieved for both raw and residual signals, indicating the framework's ability to generalize across different nozzle sources.

In particular, the real-world dataset achieves slightly higher accuracy in some cases. This is likely due to the reduced complexity of the classification task, given the smaller number of fault classes. Confusion matrices corresponding to these results are provided in Appendix C for further analysis.

3.6 Summary and Conclusion

This part of the thesis presents the development and evaluation of a framework for FDI in piezo-based industrial printing systems. The approach integrates frequency-domain feature extraction with classification techniques and is designed to operate efficiently under real-time constraints.

The proposed method extends previous work in several ways. A two-stage FDI structure is implemented, where the system first detects whether a signal is faulty and then identifies the most likely fault type. Compared to earlier approaches based on the time domain and threshold, this method shifts the analysis to the frequency domain and incorporates multiple features, such as frequency, damping, amplitude, phase, DC offset, energy, and magnitude, extracted from raw signals or residuals. These features serve as input for classifiers such as KNN and Random

Forest, allowing improved discrimination between fault classes.

The framework is evaluated using both simulated and real-world data. Classification accuracy is generally higher for features extracted from raw signals, particularly when fault characteristics involve high-frequency components. In contrast, residual-based signals provide advantages in isolating faults dominated by low-frequency dynamics. Targeted filter modifications further improve the classification performance for the residual dataset, narrowing the performance gap between the raw and residual signal representations.

Despite these improvements, the results also highlight several challenges that remain open for future work:

- **Residual signal information loss:** Although residuals are commonly used in model-based FDI, this study shows that they can lose critical high-frequency components, especially in fast or subtle fault types. Enhancing the residual filter design or combining raw and residual features may improve performance.

- **Sinusoidal assumption:** The current feature extraction method uses a fixed set of features based on sinusoidal assumptions. Although suitable for most self-sensing signals in this context, such assumptions may not hold in all real-world conditions. Future work could explore adaptive or learned features representations that better reflect the variability of real-world signals.

- **Dependence on predefined features:** The current approach relies on a predefined set of frequency-domain features. Although this simplifies the process, it may lead to the loss of useful information. For example, only the dominant frequency is extracted, even when multiple relevant components exist. This can limit the model's ability to capture the full behavior of the system. Moreover, the optimal feature set may vary depending on the fault type. Future research could investigate adaptive or data-driven feature extraction techniques that preserve more of the signal's richness.

- **Generalization to unknown faults:** The system performs well on known and labeled fault types, but may struggle with unseen or unlabeled faults. Since real-world environments often involve evolving fault conditions, future work could explore anomaly detection, semi-supervised learning, or clustering-based methods to improve robustness and adaptability.

Overall, the proposed FDI framework demonstrates promising results in terms of accuracy and computational efficiency, particularly for known and well-characterized faults. The insights gained from this work guide the next phase of the thesis, where the focus shifts from fault detection to fault estimation, reconstructing how faults evolve over time using model-based techniques.

4 PART II – Fault Estimation (FE)

Fault estimation extends the tasks of FDI by focusing on quantifying how faults develop over time. In this part of the thesis, system-theoretic methods are combined with piezo self-sensing measurements to estimate both the magnitude and evolution of faults in CPP printers. The objective is to evaluate appropriate estimation techniques and assess their potential for application in real-world industrial environments.

4.1 Transition from FDI to Fault Estimation (FE)

With the FDI system developed and evaluated, this thesis now turns to the next phase: Fault Estimation. This transition is both logical and necessary, as the FE component builds directly on the output of the FDI framework.

The process begins by passing the full dataset to the FDI block, which simultaneously determines whether each signal is faulty and, if so, assigns it to a specific fault class. This single-step approach is designed to operate with low computational complexity, making it well-suited for high-throughput or real-time applications.

To extend the diagnostic capabilities of the system, this work introduces a fault estimation block that follows the isolation step. The FE block is responsible for tracking or estimating the fault behavior over time. Unlike FDI, which apply uniformly to all fault types, estimation must be tailored to the characteristics of each specific fault class.

In this thesis, the FE method focuses on one representative fault class: the *drying nozzle*. This class is chosen due to its practical relevance and dynamic behavior. The output of the FDI system provides the necessary fault class labels, which serve as input to the FE module. Together, these components form an end-to-end framework that begins with classification and concludes with fault signal reconstruction.

The next sections present the development, implementation, and evaluation of this estimation method. Figure 16 summarizes the complete framework, from FDI to class-specific FE.

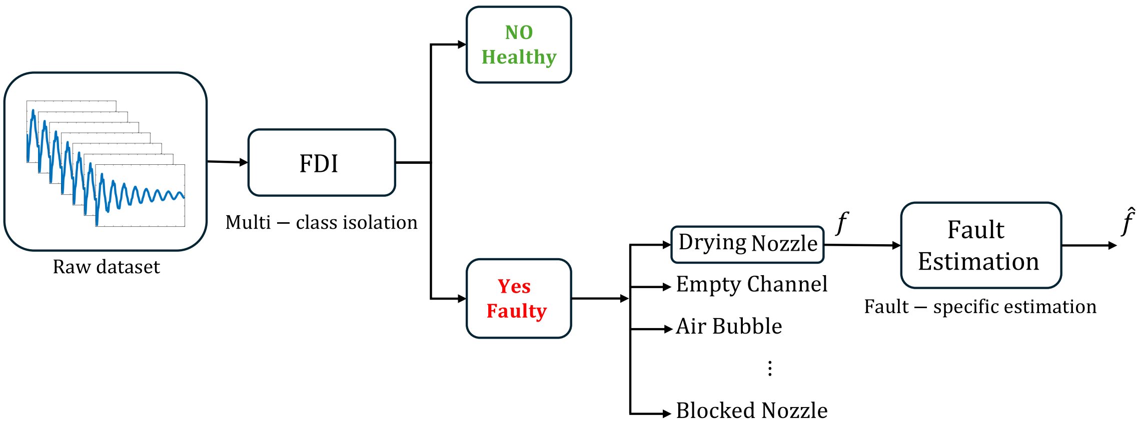

Figure 16: Overview of the complete framework from FDI to FE. The FDI blocks classify signals efficiently, while the FE block reconstructs the fault behavior for a selected fault class.

4.2 Literature Review and Existing Solutions

Fault estimation methods are commonly divided into two major categories: observer-based techniques and regression-based (or data-driven) approaches [30, 31]. Observer-based methods are more traditional and widely used when system dynamics and noise characteristics are well understood. These methods rely on constructing dynamic estimators, such as Luenberger observers, or unknown input observers, that reconstruct internal states and faults based on system models.

Regression-based techniques, on the other hand, estimate faults directly from measured signals using algebraic relations or statistical inference. These methods are often preferred when a full system model is not available, or when the relationship between inputs, outputs, and faults is too complex to be captured analytically. Compared to observer-based methods, regression approaches may offer greater flexibility in handling nonlinearities and complex data patterns.

A representative regression-based fault estimation method is proposed in [29], which combines model-based residual generation with nonlinear regression. The system is modeled using a discrete-time differential-algebraic equation (DAE) framework that captures both dynamic and algebraic relations between internal states, known signals, and fault inputs. The general form of the model is expressed as:

$$H(q)[x] + L(q)[z] + F(q)\left[f_a + E(z)f_m\right] = 0 \tag{3}$$

Here, x represents the unknown internal states and disturbances, z includes known signals (inputs and measurements), and f_a and f_m denote additive and multiplicative faults, respectively. The nonlinear function $E(z)$ captures the way multiplicative faults interact with the known signals. The term $f_a + E(z)f_m$ captures both types of faults and is referred to as the *aggregated fault signal.* The shift operator q advances a discrete-time signal by one step, i.e., $qx(k) = x(k+1)$, and is used to express system dynamics in difference form.

The objective is to design a filter that maps the known signals z to an estimate $\hat{f}$ of the actual fault vector $f = [f_a, f_m]^T$, such that the estimation error remains bounded:

$$\|f(k) - \hat{f}(k)\|_2 \leq C(C_z, C_f, k - k_0) \tag{4}$$

Here, C is an explicit bound on the model 3, the parameters C_Z and C_f are functions of measurement z and fault signal f, k_0 denotes the time the fault occurs and k is the current time.

This solution is structured into three main blocks, illustrated in Figure 17:

1. **Fault Detection Block:** Estimates the aggregated fault signal.
2. **Pre-filter Block:** Applies a linear transfer function τ to reduce dynamic mismatch between the regressor (e) and the residual (r):

$$\begin{aligned} r &= \tau \left[f_a + E(z)f_m \right] \\ \tau^{-1} r &= \left[f_a + E(z)f_m \right] \end{aligned} \tag{5}$$

3. **Fault Isolation Block:** Isolates f_a and f_m using a nonlinear regression:

$$\hat{f} = e^{\dagger} \cdot r \tag{6}$$

Although the final estimation step appears linear, the regressor e includes the nonlinear term $E(z)$, making the regression implicitly nonlinear with respect to the fault variable. This careful design allows accurate isolation of fault components.

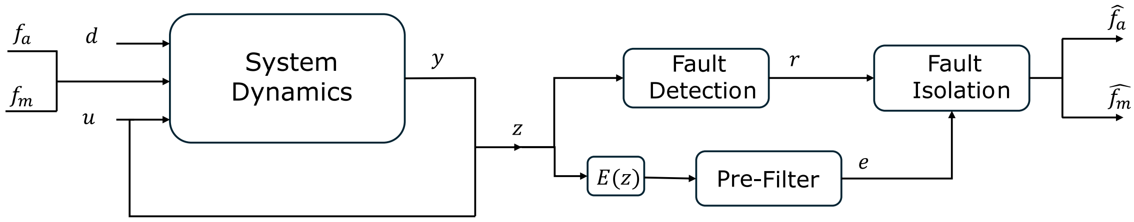

Figure 17: Block diagram of diagnosis filter.

Compared to traditional observer-based approaches [30, 31] and optimization-based methods [32], this method is lightweight and computationally efficient. It avoids iterative optimization and relies only on matrix multiplication and pseudo-inverse computation, making it highly suitable for real-time implementation in industrial systems such as Canon's high-speed printers.

However, the method assumes access to accurate input-output data and well-defined nonlinear mappings. These assumptions may not always hold in real-world settings. In contrast, the method proposed in this thesis is based on a linear, physically interpretable system model tailored to Canon's inkjet dynamics. It avoids reliance on complex nonlinear mappings, improving transparency and allowing better integration with control strategies. This makes it more practical for industrial applications that require robustness, clarity, and low computational overhead.

4.3 Proposed Solution

This section presents the proposed fault estimation framework developed for CPP printers. The approach focuses on estimating the progression of faults over time, with particular attention to the nonlinear influence of multiplicative faults on the system dynamics.

4.3.1 Problem Formulation

The first step in developing an effective estimation method is to understand the nature of faults present in CPP systems. As outlined in Appendix A, this work considers only multiplicative (parametric) faults. These faults differ from additive faults in that they alter the system's internal dynamics rather than introducing external disturbances. As a result, they typically lead to nonlinear system behavior, which complicates the design of conventional estimators or observers [29].

Among the various types of multiplicative faults, this thesis specifically focuses on faults caused by nozzle drying, referred to as *dry nozzle faults*. To make the estimation of such faults tractable, it is assumed that the fault signal varies slowly over time or is approximately piecewise constant such that the fault can be considered constant for the duration of the signal. This common assumption simplifies the estimation problem while still capturing the key behavior of the fault.

The underlying system is modeled as an autonomous continuous-time dynamic system, as described in Section 3.1. Since no simultaneous input-output data are available in CPP printers, due to the piezoelectric actuator acting both as the actuator and sensor, this formulation avoids the need for external control inputs. However, it also means that the system's initial state must be estimated manually. This is typically done by extracting representative signal features, such as amplitude, damping, and frequency, from prior measurements and using them to reconstruct a consistent initial state across simulations.

$$\underbrace{\begin{bmatrix} \dot{V}_r \\ \dot{V}_n \\ \ddot{V}_r \\ \ddot{V}_n \end{bmatrix}}_{\dot{x}} = \underbrace{\begin{bmatrix} 0 & 0 & 1 & 0 \\ 0 & 0 & 0 & 1 \\ \frac{1}{I_r B_t} & -\frac{1}{I_r B_t} & -\frac{R_r}{I_r} & 0 \\ -\frac{1}{I_n B_t} & \frac{1}{I_n B_t} & 0 & -\frac{R_n}{I_n} \end{bmatrix}}_{A} \underbrace{\begin{bmatrix} V_r \\ V_n \\ \dot{V}_r \\ \dot{V}_n \end{bmatrix}}_{x} \tag{7}$$

Experimental analysis indicates that a dry nozzle fault primarily results in an increase in the parameter R_n, which represents flow resistance due to ink viscosity. All other parameters remain unchanged. This implies that only the $(4, 4)$ element of matrix A is affected. Consequently, R_n is chosen as the primary fault variable in the estimation model.

Given that only one parameter changes under fault conditions, the system can be modeled as:

$$\dot{x} = Ax + \Delta Ax \tag{8}$$

where ΔA contains non-zero elements only at position $(4,4)$:

$$\Delta A = \begin{bmatrix} 0 & 0 & 0 & 0 \\ 0 & 0 & 0 & 0 \\ 0 & 0 & 0 & 0 \\ 0 & 0 & 0 & \frac{\Delta R_n}{I_n} \end{bmatrix} \tag{9}$$

To separate the fault from the system dynamics, the model is rewritten as:

$$\dot{x} = Ax + B_f E(x) f_m \tag{10}$$

where B_f is a fault input matrix, $E(x)$ is a nonlinear function of state x_4, and $f_m = \frac{\Delta R_n}{I_n}$. The system becomes:

$$\dot{x} = Ax + \begin{bmatrix} 0 & 0 & 0 & 1 \end{bmatrix}^T x_4 \cdot \frac{\Delta R_n}{I_n} \tag{11}$$

Because the fault term is state-dependent, it introduces nonlinear behavior into the model, which poses a challenge for estimation.

This thesis uses three different datasets, summarized in Table 8. Each dataset serves a specific purpose in evaluating the proposed methods under varying levels of realism and complexity.

Dataset	Description
Synthetic Data	Simulated data generated from identified linear system dynamics. Used to validate models under controlled, noise-free conditions.
Physics-Based Data	Data derived from nonlinear physical equations representing Canon printer systems. Provides more realistic dynamics while retaining a model-based foundation.
Real Data	Measurement data collected directly from Canon printers operating under real-world conditions.

Table 8: Summary of the three datasets used in this thesis.

4.3.2 Observability & Validation of Identified Linear Model

A central challenge in estimating f_m is that x_4 is not directly measurable. Since the system output is a linear combination of x_3 and x_4, the internal states are not fully observable. Furthermore, standard state observers cannot be used, as the fault acts as an unknown input.

To address this, a reformulated state-space model is introduced by combining the first and second states to create an observable system:

$$
\begin{aligned}
\underbrace{\begin{bmatrix} \dot{V}_r + \dot{V}_n \\ \ddot{V}_r \\ \ddot{V}_n \end{bmatrix}}_{\dot{x}} &= \underbrace{\begin{bmatrix} 0 & 1 & 1 \\ \frac{1}{I_r B_t} & -\frac{R_r}{I_r} & 0 \\ -\frac{1}{I_n B_t} & 0 & -\frac{R_n}{I_n} \end{bmatrix}}_{A} \underbrace{\begin{bmatrix} V_r + V_n \\ \dot{V}_r \\ \dot{V}_n \end{bmatrix}}_{x}, \\
y &= \underbrace{\begin{bmatrix} 0 & 1 & 1 \end{bmatrix}}_{C} \underbrace{\begin{bmatrix} V_r + V_n \\ \dot{V}_r \\ \dot{V}_n \end{bmatrix}}_{x}
\end{aligned}
\tag{12}
$$

To evaluate the adequacy of the linear model, this study compares synthetic data with real data. Figure 18 shows the relationship between dominant frequency and damping ratio for both the identified model and the fault data collected from CPP printers. The close match between the system dynamics of model and real data suggests that the identified linear model sufficiently captures the system's behavior under fault conditions and can be used to develop the estimation framework.

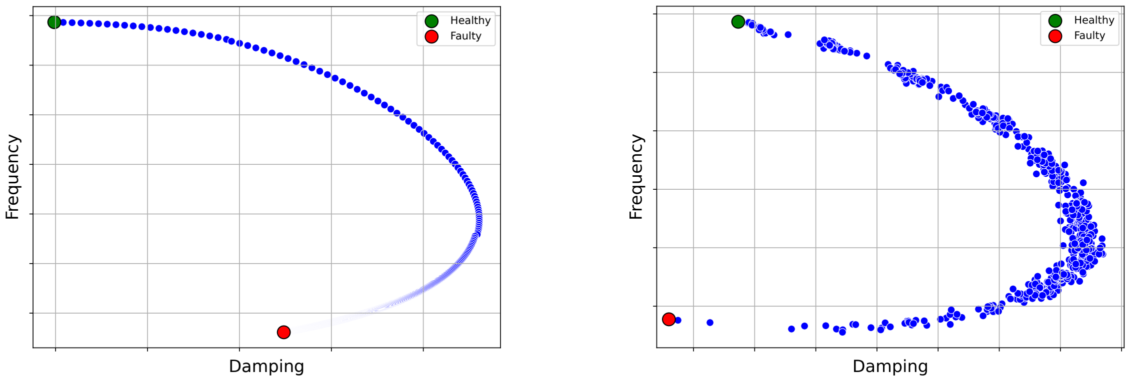

(a) Simulated data from the linear model.

(b) Real data under fault conditions.

Figure 18: Comparison of the Frequency–Damping relationship for simulated and real data.

4.3.3 Design of the Unknown Input Observer (UIO)

Standard observers typically assume that all system inputs are known. As a result, their estimates can become biased when unknown disturbances or faults are present [32]. In contrast, UIOs are specifically designed to decouple the influence of unknown inputs from the state estimation process [33]. This makes them particularly well suited for fault-tolerant estimation in systems like Canon printers, where faults influence internal states without direct control inputs.

Figure 19 illustrates the conceptual difference between a standard observer and a UIO.

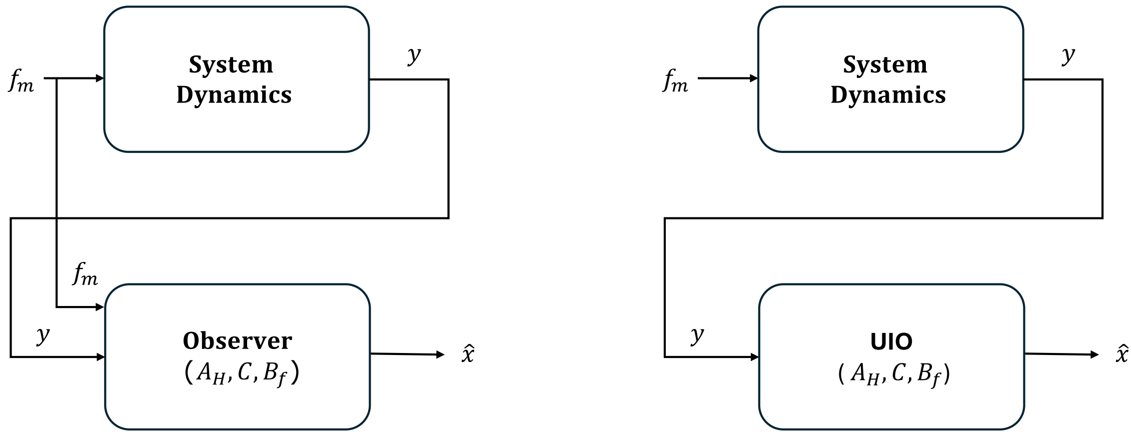

Figure 19: Block diagram comparison between a standard observer and an UIO.

The faulty system of CPP printers, using the observable model (12) is described in state-space form as follows:

$$\begin{aligned} \dot{x}(t) &= Ax(t) + B_f \underbrace{f_m x_3(t)}_{f(t)}, \\ y(t) &= Cx(t), \end{aligned} \tag{13}$$

where $x(t) \in \mathbb{R}^n$ is the system state vector, $f(t) = f_m x_3(t)$ represents the unknown input (fault), $B_f \in \mathbb{R}^{n\times 1}$ is the fault input matrix, and $C \in \mathbb{R}^{p\times n}$ is the output matrix. Since the system operates autonomously, no control input is included.

The UIO is designed to estimate the system's internal states $\hat{x}$ using only the output signal y, while rejecting the unknown input $f(t)$. The observer reconstructs the state x_3, which plays a key role in computing the nonlinear term $E(x)$ and estimating the fault magnitude f_m. The observer structure is defined as:

$$\begin{aligned} \dot{z} &= Fz + Ty, \\ \hat{x} &= z + Hy \end{aligned} \tag{14}$$

where $z \in \mathbb{R}^n$ is the observer's internal state and the matrices F, T, H must be designed such that the estimation error is insensitive to the unknown input [33]. To eliminate the effect of the unknown input, the estimation error is defined as follows:

$$e = x - \hat{x} = x - z - Hy. \tag{15}$$

Differentiating and substituting $x = e + z + Hy$ the system dynamics, we derive the following.

$$\begin{aligned} \dot{e} = \dot{x} &- \dot{z} - H\dot{y}, \\ &= Ax + B_f f - Fz - Ty - HC\dot{x}, \\ &= (A - HCA)e + (A - F - HCA)z \\ &\quad + (AH - T - HCAH)y + (I - HC)B_f f.. \end{aligned} \tag{16}$$

To ensure robustness, the estimation error $\dot{e}$ must remain bounded and ideally converge to zero. This is achieved by eliminating the influence of z, y, and the unknown input $f(t)$ from the error dynamics. To decouple the error from the fault input, the following condition is imposed:

$$(I - HC)B_f = 0 \quad \Rightarrow \quad HCB_f = B_f. \tag{17}$$

Once the matrix H is determined to satisfy the decoupling condition, the observer matrices F and T are selected to ensure stable and consistent error dynamics. Specifically, the matrix F is defined as:

$$F = A - HCA, \tag{18}$$

This choice eliminates the dependence of the estimation error $\dot{e}$ on the internal observer state z. If $\dot{e}$ depends on z, the internal dynamics of the observer may introduce additional estimation errors. By removing the z-term, the error dynamics become simpler, more predictable, and easier to stabilize.

Similarly, to eliminate the term $(AH - T - HCAH)y$. from the error dynamics, the following condition is imposed:

$$T = AH - HCAH. \tag{19}$$

This ensures that the output correction term Hy evolves in a way that matches the system's natural behavior. As a result, the observer's output-based correction more accurately reflects the system dynamics, improving estimation quality and simplifying the observer structure. However, in many practical applications, it is common to simplify this design by approximating:

$$T = AH. \tag{20}$$

This approximation makes the injection matrix T consistent with the nominal dynamics as seen through the correction gain H, while avoiding unnecessary compensation terms. It is a practical and widely accepted approach in the literature.

The matrix H is determined using the Moore–Penrose pseudoinverse, expressed as $H = B_f(CB_f)^\dagger$. This formulation is valid under the condition that $\text{rank}(CB_f) = \text{rank}(B_f)$, ensuring that the influence of the unknown input on the state is observable in the output.

The final UIO structure, as presented in (14), enables estimation of the full system state $\hat{x}$, independently of the fault signal $f(t)$. Once the relevant state (e.g., x_3) is estimated, it can be used to compute the nonlinear fault term $E(x)f_m$ for fault reconstruction.

The performance of the proposed UIO is illustrated in Figure 20. The estimated states closely follow the true system states, even in the presence of an unknown fault input. The high fit percentage demonstrates the effectiveness of the UIO for the application.

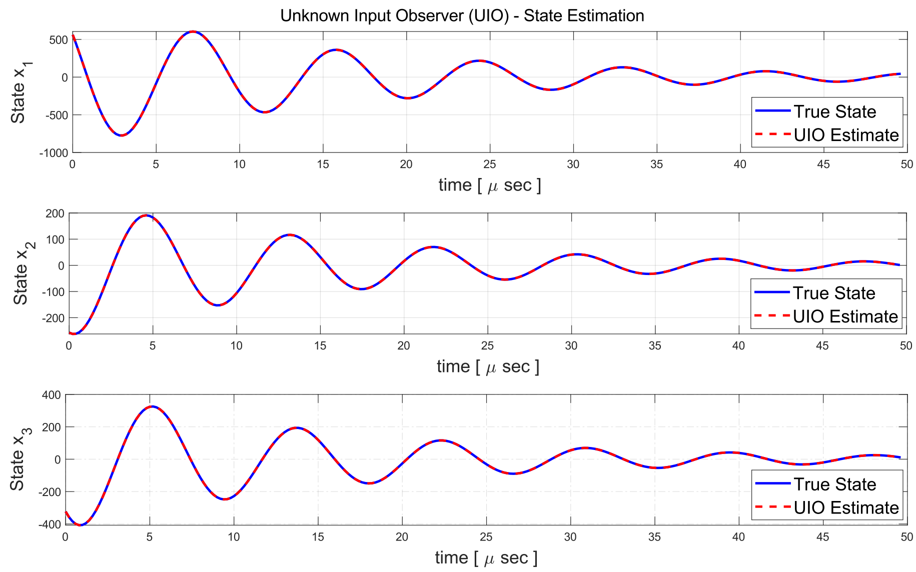

Figure 20: State estimation results using the UIO. (dashed lines) track the true system states (solid lines), confirming robustness to the unknown fault input.

4.3.4 Modeling Considerations and Estimation Framework

A key modeling challenge in fault estimation arises from the transition between continuous- and discrete-time representations. The Canon printer system is originally described in continuous time, where the multiplicative fault, represented by a variation in the parameter ΔR_n, affects only a single entry in the system matrix A. This localized effect allows for clearer interpretation of fault influence in the continuous domain.

However, the fault estimation framework adopted in this work, based on [29], operates in discrete time. This is mainly due to the structure of the regression-based fault isolation block, which is more tractable and stable when applied to discrete-time data. Additionally, working in discrete time avoids the need for complex operations such as deconvolution, which are typically required in continuous-time implementations.

Although the discrete-time framework simplifies the application of regression techniques, discretizing the system introduces new complications. Specifically, the fault effect, which is isolated to a single element in the continuous-time matrix A, becomes distributed across multiple elements in the discrete-time matrix after standard discretization. This transformation can distort the original fault structure, making it harder to interpret and track the fault influence accurately.

To address this challenge, two alternative strategies are proposed:

1. **Discrete-Time (DT) Approach:** The continuous-time system is fully discretized, and fault estimation is performed directly on the resulting discrete-time model. This approach assumes that the essential fault structure remains preserved during discretization. However, particular care is required to ensure that the fault's influence on the system dynamics is not significantly altered in the process.

2. **Continuous-Time (CT) Approach:** In this strategy, the system dynamics are retained in continuous time, and only the system output is discretized. This allows the regression-based estimation block to operate in discrete time while maintaining the simpler, more interpretable fault structure of the continuous-time model. The key challenge here lies in ensuring that the numerical integration and output sampling are accurate enough to avoid introducing significant errors.

Figure 21 shows the block diagram of the proposed fault estimation framework. The goal is to estimate the fault magnitude over time, based solely on observed output signals and internal state estimates.

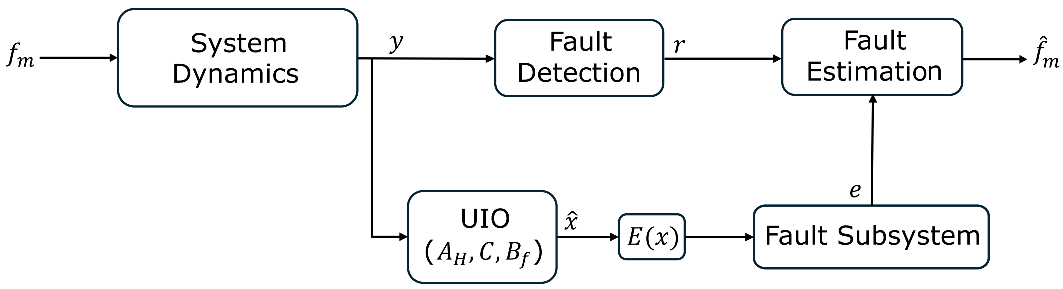

Figure 21: Block diagram of the proposed fault estimation architecture.

The framework consists of three main components:

- **Fault Detection Block:** This block compares the model-based output with measured signals to compute a residual. The residual reflects the combined effect of the fault term $E(x)f_m$.

- **Fault Subsystem Block:** This block acts as a transfer function that compensates for dynamic mismatches between the true fault input and the observed residual. It improves fault estimation accuracy by correcting for any distortions introduced earlier in the process.

- **Fault Estimation Block:** A regression operator is applied to extract the fault magnitude f_m from the residual. This step isolates the fault effect by leveraging the structure of the fault signal.

Discrete-Time Fault Estimation Approach

In the DT approach, the entire system, including the state-space model and estimation framework, is formulated in discrete time. The main challenge in this approach lies in discretization of the continuous-time model in a way that preserves the fault's structural influence, particularly its effect on the A matrix.

The observable continuous-time model introduced in (12) is extended to include a fault-dependent term arising from the variation ΔR_n. The faulty system dynamics is then written as:

$$\dot{x} = \underbrace{\left(\underbrace{\begin{bmatrix} 0 & 1 & 1 \\ -\frac{1}{I_r B_t} & -\frac{R_r}{I_r} & 0 \\ -\frac{1}{I_n B_t} & 0 & -\frac{R_n}{I_n} \end{bmatrix}}_{A_H^{CT}} + \underbrace{\begin{bmatrix} 0 & 0 & 0 \\ 0 & 0 & 0 \\ 0 & 0 & \frac{\Delta R_n}{I_n} \end{bmatrix}}_{\Delta A} \right)}_{A_f^{CT}} x \tag{21}$$

To convert the continuous-time system into a discrete-time model, the matrix exponential is commonly used. Specifically, the discrete-time system matrix A_f^{DT} is obtained from the continuous-time system matrix A_f^{CT} using the relationship:

$$A_f^{DT} = e^{A_f^{CT} \cdot \mathrm{d}t} \tag{22}$$

This relationship arises from the analytical solution of linear time-invariant (LTI) systems, where the matrix exponential describes the state evolution over a sampling interval dt. However, when the system matrix includes a fault term ΔA, the expression becomes:

$$A_f^{DT} = e^{(A_H^{CT}+\Delta A)\cdot \mathrm{d}t} \tag{23}$$

Due to the non-commutative nature of matrix multiplication, this cannot be decomposed into a simple sum of exponentials, i.e., $e^{A_H^{CT}\cdot \mathrm{d}t} + e^{\Delta A\cdot \mathrm{d}t}$. As a result, the fault influence, which originally affects only one element in A, becomes distributed across multiple elements in the discrete-time matrix in a nonlinear manner, complicating fault estimation.

To address this issue, an approximation is introduced in which only the healthy system matrix A_H^{CT} is discretized, while the fault term ΔA is added in as in continuous form, scaled by dt:

$$A_f^{DT} \approx e^{A_H^{CT}\cdot \mathrm{d}t} + \begin{bmatrix} 0 & 0 & 0 \\ 0 & 0 & 0 \\ 0 & 0 & \frac{\Delta R_n}{I_n}\cdot \mathrm{d}t \end{bmatrix} \tag{24}$$

Under this approximation, the faulty system dynamics in discrete time become:

$$\begin{aligned} x(k+1) &= \underbrace{e^{A_H^{CT}\cdot \mathrm{d}t}}_{A_H^{DT}} x(k) + \underbrace{\begin{bmatrix} 0 & 0 & 1 \end{bmatrix}^T}_{B_f} \underbrace{x_3(k)}_{E(x_3)} \cdot \underbrace{\frac{\Delta R_n}{I_n}}_{f_m} \cdot \mathrm{d}t \\ y(k) &= \underbrace{\begin{bmatrix} 0 & 1 & 1 \end{bmatrix}}_{C} x(k) \end{aligned} \tag{25}$$

Here, $x(k) \in \mathbb{R}^3$ denotes the state vector at time step k, and $y(k)$ is the system output. The term $x_3(k)$ represents the third state variable, which is affected by the fault. The influence of the fault is preserved in the form $E(x_3)\cdot f_m$, where $f_m = \frac{\Delta R_n}{I_n}$.

This approximation is motivated by the Taylor series expansion of the matrix exponential. By retaining lower-order terms, the effect of ΔR_n remains explicitly represented and more interpretable in the discrete model. A detailed derivation of the Taylor-based approximation is provided in Appendix E.

After discretization, all steps in the fault detection and estimation pipeline, including residual generation and regression, are carried out in discrete time. The complete workflow is summarized in the block diagram below.

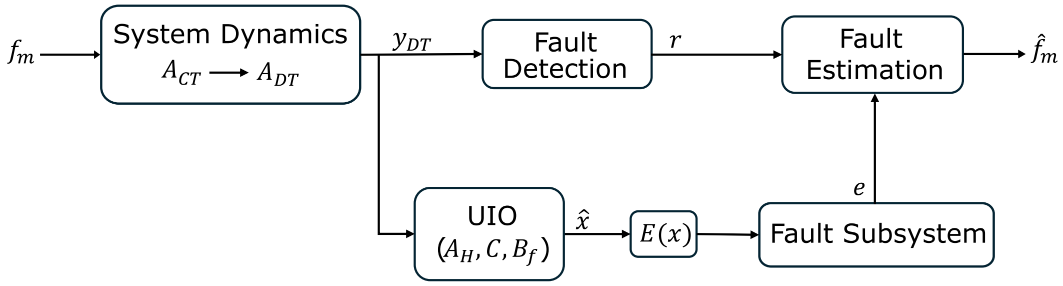

Figure 22: Block diagram of the discrete-time fault estimation approach. The entire system is modeled and processed in discrete time. Special attention is given to preserving the fault structure during discretization.

Continuous-Time Fault Estimation Approach

In the CT approach, the system is modeled and simulated using its original continuous formulation. This strategy preserves the localized effect of the fault on the system matrix A, particularly the influence of ΔR_n on a single matrix element. Maintaining the continuous-time structure enables a more accurate representation of the system dynamics prior to any discretization.

The faulty system is represented by the following state-space equations:

$$\begin{aligned}
\dot{x}(t) &= A_H^{CT} x(t) + \underbrace{\begin{bmatrix} 0 & 0 & 1 \end{bmatrix}^T}_{B_f} \underbrace{x_3(t)}_{E(x)} \cdot \underbrace{\frac{\Delta R_n}{I_n}}_{f_m} \\
y(t) &= \underbrace{\begin{bmatrix} 0 & 1 & 1 \end{bmatrix}}_{C} x(t)
\end{aligned} \tag{26}$$

Here, $x(t) \in \mathbb{R}^3$ is the system state vector, and $x_3(t)$ is the third state, which appears in the fault term as part of the multiplicative structure. The output $y(t)$ is a linear combination of the second and third states, in line with the self-sensing measurement of the Canon system.

During simulation of the CT approach, the output $y(t)$ is sampled at regular intervals to generate a discrete-time signal. This enables the use of discrete-time fault estimation algorithms without the need to discretize the entire system model. By avoiding full system discretization, the localized structure of the fault is retained, which simplifies interpretation and improves isolability.

A central challenge in this approach lies in accurately discretizing the output while minimizing numerical integration errors. To achieve this, the system output is integrated using MATLAB's `ode45` solver, which implements an adaptive Runge–Kutta (4,5) method. During each sampling interval of length $\mathrm{d}t$, corresponding to Canon's system sampling rate, the output is simulated over the interval $[(k-1)\mathrm{d}t,\ k\mathrm{d}t]$. The solver internally uses smaller adaptive time steps, but only the final value at $t = k \cdot \mathrm{d}t$ is retained. This output sample is used as the discrete-time output.

This procedure ensures that the output is aligned with the discrete-time fault estimation framework while preserving the fidelity of the original continuous-time dynamics. The resulting signal is then processed using the same regression-based fault detection and estimation steps as in the DT approach.

The overall structure of the CT-based estimation method is shown in the block diagram below.

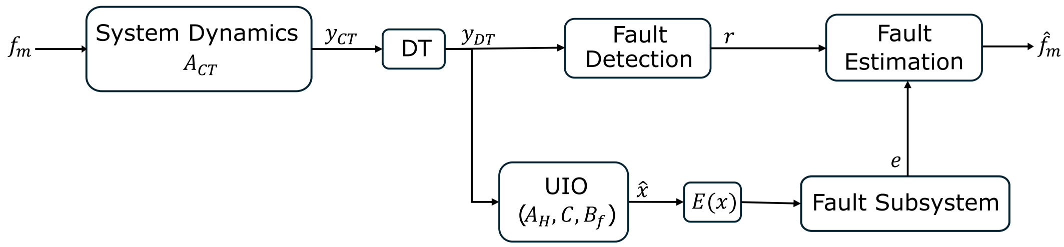

Figure 23: Block diagram of the continuous-time fault estimation approach. The system is simulated in continuous time, and the output is sampled for discrete-time fault estimation.

4.4 Results on Synthetic Data

This section presents the performance of the proposed fault estimation framework using synthetic data. Both the DT and CT approaches are evaluated in estimating a multiplicative fault, and their results are compared across various fault levels.

4.4.1 Description of the Synthetic Dataset

The synthetic dataset is generated by simulating the faulty system dynamics in both DT and CT, as described in (25) and (26). The objective is to produce a controlled dataset in which the true fault values are known, allowing for a clear and quantifiable evaluation of estimation performance.

The fault magnitudes (f_m) used in the simulations are derived from the true fault values obtained from a physics-based model of Canon printers, as discussed in Section 4.5. A detailed explanation of how these values are computed is provided in Appendix F. Since f_m [s^{-1}] is directly proportional to the change in dynamic viscosity, $\Delta\mu$, , it serves as a physically interpretable indicator of the drying nozzle fault.

Each simulation applies a known f_m value to the system model,producing a dataset that contains 49 distinct fault levels. These levels span a wide range of fault severities in the system's output.

All simulations are performed using time units in microseconds (μs), with a sampling interval that matches Canon's printer hardware, denoted by dt. Although in practice each measurement may begin from a different initial state, it is assumed in these simulations that all signals start from the same manually estimated initial condition. This assumption simplifies the analysis while still reflecting the typical behavior observed in self-sensing measurements, which the simulations follow over a similar time period.

This dataset enables consistent and repeatable evaluation of the proposed fault estimation method under idealized conditions. It helps identify both strengths and limitations of the approach before applying it to more complex scenarios involving real-world signals.

4.4.2 Fault Estimation using the DT Approach

The performance of the DT fault estimation method is illustrated in Figure 24 and Figure 25. In Figure 24 (top), the estimated fault signal $f_{m_{\mathrm{est}}}$ (red) closely follows the true fault f_m (blue), with an error on the order of 10^{-6}. The zoomed-in view highlights this close agreement, demonstrating the estimator's precision in tracking fault dynamics.

The lower plot in Figure 24 shows the logarithm of the absolute estimation error, $\log(|f_m - \hat{f}_m|)$, over time. Initially, the error is relatively large as the estimator adjusts to the system's dynamics. However, it quickly decreases and stabilizes, confirming that the DT estimator adapts effectively after a short transient period.

Figure 25 presents the estimation accuracy across a range of synthetic signals with varying fault magnitudes. The x-axis indicates the fault level (0–100), while the y-axis shows the estimation accuracy in (%) as the average fit during the steady-state condition of each signal. Although a slight decrease in accuracy is observed at higher fault levels, all values remain above 99%, indicating robust performance.

One possible explanation for the minor downward drift observed in Figure 24, as well as the small accuracy drop in Figure 25, relates to the discretization assumptions described in Section 4.3.4. The method assumes that the fault's influence remains unchanged when transitioning from continuous to discrete time. Although this simplifies the modeling, it may neglect nonlinear behaviors, leading to small estimation biases.

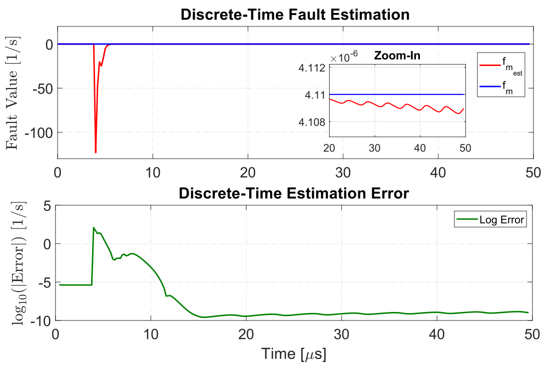

Figure 24: Fault estimation using the discrete-time approach for a single signal.

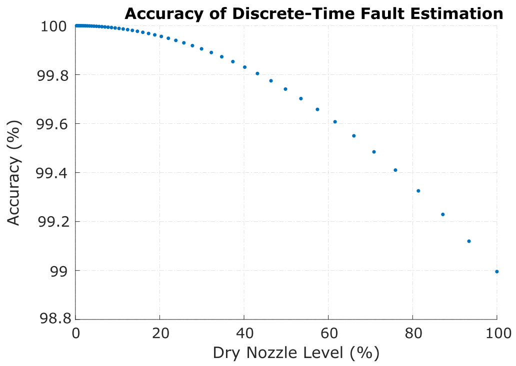

Figure 25: Fault estimation accuracy across varying fault levels (Dry Nozzle Level) using the discrete-time approach.

4.4.3 Fault Estimation using the CT Approach

The CT estimation results are shown in Figure 26 and Figure 27. In Figure 26, the estimated fault signal closely tracks the ground truth, although it exhibits slightly higher oscillations compared to the DT case. These oscillations are likely caused by the numerical errors introduced during output discretization.

Figure 27 summarizes the estimation accuracy across multiple synthetic signals with increasing fault magnitudes. A gradual, approximately linear decline in accuracy is observed as fault severity increases. Nevertheless, the accuracy remains above 98% for all tested cases, indicating robustness of the CT method.

The observed performance drop is attributed to the structure of the CT approach, where only the output is discretized while the system dynamics remain in continuous form. This allows for higher model fidelity but introduces numerical challenges, particularly during signal sampling. Discretization errors may reduce signal quality and slightly degrade estimation accuracy.

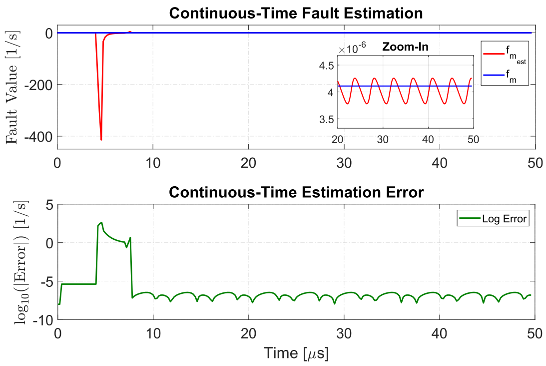

Figure 26: Fault estimation using the continuous-time approach for a single signal. The estimated signal tracks the ground truth with slightly higher oscillation due to output discretization.

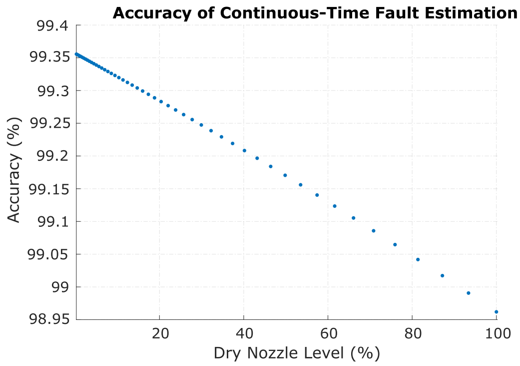

Figure 27: Fault estimation accuracy across varying fault levels (Dry Nozzle Level) using the continuous-time approach. Accuracy remains above 98%, though a linear drop is observed for larger faults.

In summary, both methods perform well on synthetic data, each offering different advantages. The DT approach yields slightly higher fit accuracy, whereas the CT approach maintains greater structural fidelity to the original model. These findings suggest a trade-off between numerical implementation and model clarity that may be important to consider when selecting a fault estimation strategy.

4.5 Evaluation on Physics-Based Model Data

Following the validation on synthetic data, the proposed fault estimation method is further evaluated using signals generated by a physics-based model. This dataset is derived from nonlinear physical equations of Canon printers, better reflects the dynamics of real-world systems, and thus provides a more realistic benchmark for evaluating estimator performance.

Compared to synthetic data, the estimation results in the physics-based dataset are more variable. Although the method provides a reasonable estimation for some signals, performance degrades for others, even when their overall waveform or frequency content appears similar. One contributing factor may be the identified linear structure assumed in the fault estimation model, whereas the physics-based signals exhibit nonlinear changes in response to fault magnitudes. This discrepancy between the fault's true behavior and its linear approximation may contribute to reduced estimation accuracy, especially for more severe faults. Moreover, some underperformance is observed even at lower fault levels, suggesting that other, possibly unmodeled, system properties may also play a role.

Another limitation relates to the regression-based nature of the estimator. Its performance depends on the conditioning of the associated regression matrix. If the matrix becomes poorly conditioned, the estimation may become sensitive to numerical noise and less robust.

Overall, the physics-based results help to highlight the method's limitations in terms of generalization and robustness. Although the approach shows potential under controlled conditions, these observations point to areas where the model or estimation framework may require refinement for improved performance in real-world scenarios. The following figures illustrate estimation results using both DT and CT approaches for selected signals where the method produced comparatively better outcomes.

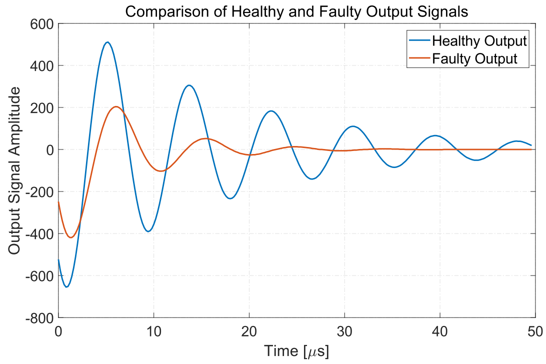

Figure 28: Healthy vs. slightly dried faulty output. Severely increased damping is visible.

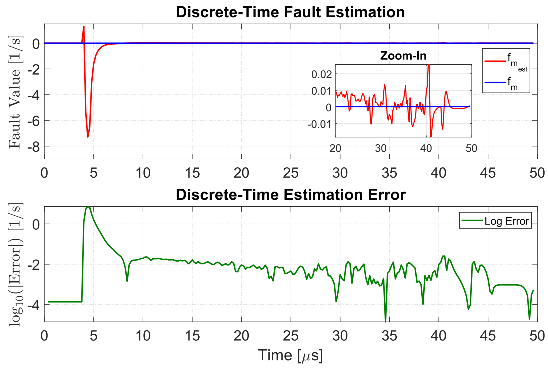

Figure 29: DT estimation for the corresponding faulty signal. The estimate reflects the fault trend with moderate deviation (92.94%).

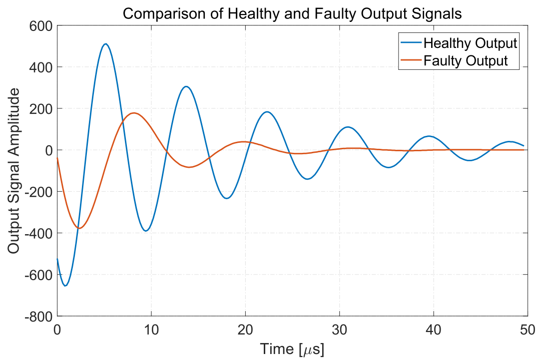

Figure 30: Healthy vs. Intermediately dried faulty output. Moderate damping is observed.

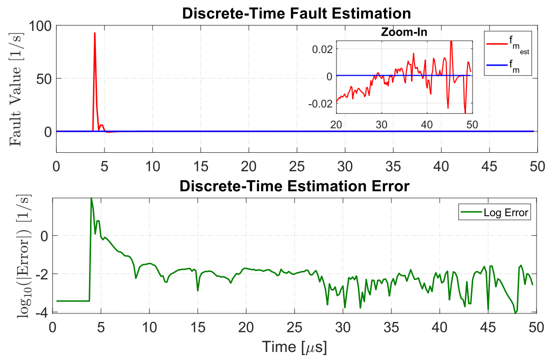

Figure 31: DT estimation for the corresponding faulty signal. The result shows relatively stable alignment with the fault (99.52%).

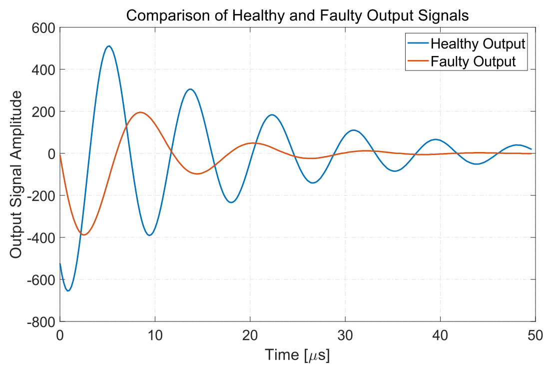

Figure 32: Healthy vs. Intermediately dried faulty output. The waveform remains smooth with moderate damping.

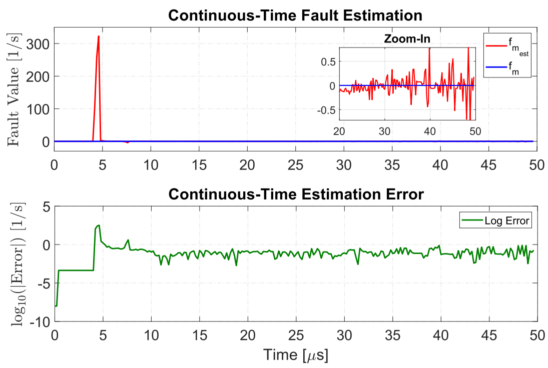

Figure 33: CT estimation for the corresponding faulty signal. The estimate generally follows the trend, though with more fluctuation (89.38%).

The DT results (Figures 29 and 31) indicate that the estimator follows the main fault trend with reported accuracies of 92.94% and 99.52%, respectively. However, the estimates show more noticeable deviations and oscillations compared to those obtained on synthetic data.

Similarly, the CT result in Figure 33 shows that, despite noticeable fluctuations, the estimated fault remains reasonably close to the true profile, with an accuracy of 89.38%.

4.6 Summary and Conclusion

This part of the thesis has investigated fault estimation techniques for Canon's high-end industrial printers, with a particular focus on estimating the progression of multiplicative fault over time. Two estimation strategies have been developed and evaluated: DT approach and a CT approach. Both rely on a physically identified linear model, and the estimators are built using a regression-based structure.

Simulation results on synthetic data suggest that both approaches are able to estimate fault signals with a high degree of accuracy under controlled conditions. In these cases, where the system dynamics are fully known and the fault follows the assumed structure, the estimation is reliable and stable. These results indicate that the linear model, combined with the proposed estimation framework, can be effective within idealized settings.

However, when the same methods are applied to a physics-based dataset, designed to better reflect real-world printer behavior, performance becomes more varied. Although fault estimates for some signals remain close to the expected values, others show clear deviations. These inconsistencies suggest that several practical factors may influence the estimation, including:

- The system identification process is based on a linear model. Although this is adequate for controlled, synthetic data, it may not account for the full complexity of the real printer dynamics.
- The manual initialization of internal states. Since the system is modeled as autonomous, the initial state must be estimated manually, typically by averaging typical signal features. However, in real-world measurements, signals often begin from unknown or varying initial conditions. Relying on a single

averaged estimate across all signals can introduce inconsistencies and reduce the robustness of the estimation.

- The approximation of fault behavior, which may not fully capture the system's response.
- The sensitivity of the regression to signal properties and the conditioning of the regression matrix. If the matrix becomes ill-conditioned, small changes in the signal can lead to large estimation errors.

In particular, the discretization method used in the DT approach assumes that the influence of the fault can be separated from the system dynamics. To make this feasible, an approximation is introduced where only the healthy part of the system matrix is discretized. Although this helps preserve the structure needed for fault estimation, it may introduce modeling errors, especially when the fault has a stronger or more complex influence on the system behavior.

Similarly, in the CT approach, the system is modeled in continuous time, but the outputs are sampled at discrete intervals. Despite the fact that this avoids structural distortion during discretization, it introduces numerical challenges. These include integration errors, especially when the magnitude of the fault grows.

Taken together, these findings highlight the trade-offs between model simplicity and estimation robustness. The proposed framework shows promise for applications where model assumptions are valid and signal conditions are favorable. At the same time, the results emphasize the need for more flexible and resilient estimation techniques when moving toward real-world deployment.

Future work may focus on:

- improving model fidelity by incorporating more dynamic effects,
- refining initial state estimation procedures,
- and exploring adaptive or learning-based fault estimation methods that can better accommodate variability in system behavior.

5 Summary of Key Contributions

This thesis presents a fault diagnosis framework for high-end industrial inkjet printing systems, with a focus on the detection, isolation, and estimation of nozzle-related faults. The research is motivated by the need to improve system reliability and minimize downtime in Canon Production Printing (CPP) machines, where unresolved nozzle faults can lead to visible print defects and operational inefficiencies.

In the first part, a modular Fault Detection and Isolation (FDI) system is developed. Unlike traditional threshold-based methods, which typically rely on residual energy alone, the proposed approach operates in the frequency domain and extracts multiple features, such as dominant frequency, amplitude, damping, and phase, from piezo self-sensing signals. These features are used to train classifiers (e.g., k-Nearest Neighbors and Random Forest), enabling the system to distinguish between several fault types. Experiments on both raw signal data and model-based residuals indicate that raw signals generally provide better classification performance, particularly for faults with higher frequency characteristics. The final FDI pipeline is computationally efficient and designed for real-time deployment.

The second part of the thesis addresses Fault Estimation (FE), with the goal of reconstructing the fault signal over time. Two estimation frameworks, discrete-time (DT) and continuous-time (CT), are proposed based on linearized system dynamics. These methods are first validated on synthetic datasets, where they show good tracking performance under idealized conditions. However, evaluation on more realistic, physics-based data reveals important limitations. Estimation accuracy varies significantly across signals, particularly due to differences in initial conditions, frequency content, and the conditioning of the regression matrix. In some cases, the simplified multiplicative fault model fails to capture complex system behavior.

Overall, this thesis contributes a unified fault diagnosis pipeline that integrates classification and estimation using a combination of model-based and data-driven tools. Although the results highlight the feasibility of applying linear models in controlled settings, they also underscore the complexity of achieving reliable fault diagnosis under realistic conditions. The work lays a foundation for future research into more robust and scalable diagnostic systems for industrial inkjet printing environments.

6 Conclusions and Future Work

This thesis investigates fault diagnosis in piezoelectric inkjet printers by developing methods for both fault detection and fault estimation. While the proposed techniques demonstrated promising results, several limitations have emerged that highlight important directions for future research.

A primary limitation in the Fault Detection and Isolation (FDI) stage is the reliance on sinusoidal-based feature extraction. Although this method performs well for many fault types, it may fail to capture non-sinusoidal or transient behaviors, particularly in residual signals, where key diagnostic information is often lost. Furthermore, the use of fixed features, such as dominant frequency or damping, does not always generalize across varying fault conditions. More adaptive or data-driven extraction methods may help preserve richer signal characteristics and improve classification performance.

Another challenge is the system's dependence on supervised learning, which requires labeled data for each known fault class. In practical industrial environments, faults often evolve or appear in forms not seen during training. This limits the system's ability to generalize to previously unseen or unlabeled faults. To address this, future research should consider semi-supervised, unsupervised, or anomaly detection approaches that increase adaptability and broaden fault coverage.

A key limitation in the second part of this thesis, which focuses on Fault Estimation (FE), lies in the reliance on simplified linear models to approximate system dynamics. Although these models have shown adequate performance on synthetic data, they struggle to maintain accuracy when applied to more realistic, physics-based datasets. This drop in performance reflects the inherent mismatch between linear assumptions and the nonlinear behaviors observed in real printer systems. In particular, nonlinear fault interactions, time-varying parameters, and unmodeled dynamics introduce estimation errors that the current approach cannot fully account for. These issues point to the need for more advanced modeling techniques that better capture the underlying system behavior under fault conditions.

In particular, the discrete-time method assumes that the fault's influence remains constant through discretization, which is not always valid for nonlinear systems. This assumption introduces distortion and reduces estimation fidelity. The continuous-time approach, although free from this discretization issue, suffers from numerical errors introduced during output sampling. These errors become more pronounced for signals affected by rapid or large-magnitude faults, degrading estimation quality.

A further limitation lies in the handling of initial system states. The current method applies a single manually estimated initial state across all signals. However, in practice, initial conditions often vary significantly between measurements. This mismatch introduces estimation error and limits the generalizability of the approach. Incorporating adaptive or signal-specific initialization strategies could improve robustness.

Future work should address the identified limitations through the following directions:

- **Adaptive Feature Extraction:** Integrating flexible, data-driven approaches for feature extraction, particularly from residual signals, may help capture a wider range of fault behaviors and improve detection sensitivity.
- **Generalization to Unlabeled Faults:** Employing semi-supervised or unsupervised learning methods, such as clustering, anomaly detection, or self-supervised models, could allow the system to detect and adapt to fault conditions not observed during training.
- **Nonlinear Modeling:** Replacing or augmenting the linear system model with nonlinear or hybrid models may increase estimation accuracy for complex and variable real-world faults.
- **Robust Initial State Estimation:** Automating the initialization process through observers, optimization techniques, or filtering methods (e.g., Kalman filters) could improve robustness and generalization across varying conditions.

In conclusion, this thesis presents a complete and modular framework for fault diagnosis in piezoelectric inkjet printers. The work integrates model-based and data-driven methods to support both detection and estimation, using a scalable and computationally efficient pipeline. At the same time, the study identifies key limitations related to modeling assumptions, generalizability, and scalability. Addressing these open challenges remains essential for translating this framework into practical and reliable diagnostic tools for industrial environments.

Appendix

A Overview of Fault Classes Used in the Experiments

This experiment considers a broader set of fault classes than those presented in [34]. As a result, some differences in performance compared to that study are to be expected. The nozzle fault types used, along with the number of samples allocated for training and testing, are summarized in Table 9.

All faults included in this analysis are modeled as multiplicative faults. These faults primarily affect the signal by modifying its amplitude or altering its shape, and serve as a basis for evaluating the classification and estimation methods proposed in this work.

Current Faulty Classes	**Type of fault**	**Numbers of Samples**	
		Training set	**Test set**
OK signals	-	250	250
Healthy Nozzle	-	250	250
Empty Channel 1	Multiplicative	250	250
Empty Channel 2	Multiplicative	250	250
Mature Air Bubble	Multiplicative	250	250
Intermediate Air Bubble	Multiplicative	250	250
Small Air Bubble	Multiplicative	250	250
Fully Blocked Nozzle	Multiplicative	250	250
Partially Blocked Nozzle	Multiplicative	250	250
Slightly Dried Nozzle	Multiplicative	250	250
Intermediately Dried Nozzle	Multiplicative	250	250
Deeply Dried Nozzle	Multiplicative	250	250

Table 9: List of fault classes used in the fault isolation experiments. All data are synthetically generated using a model of the Canon printing system. The table reports the fault type and the number of training and test samples per class.

B Confusion Matrices for Simulation Dataset Classification

This section presents the confusion matrices corresponding to the classification results summarized in Table 2, for both FD and FI tasks.

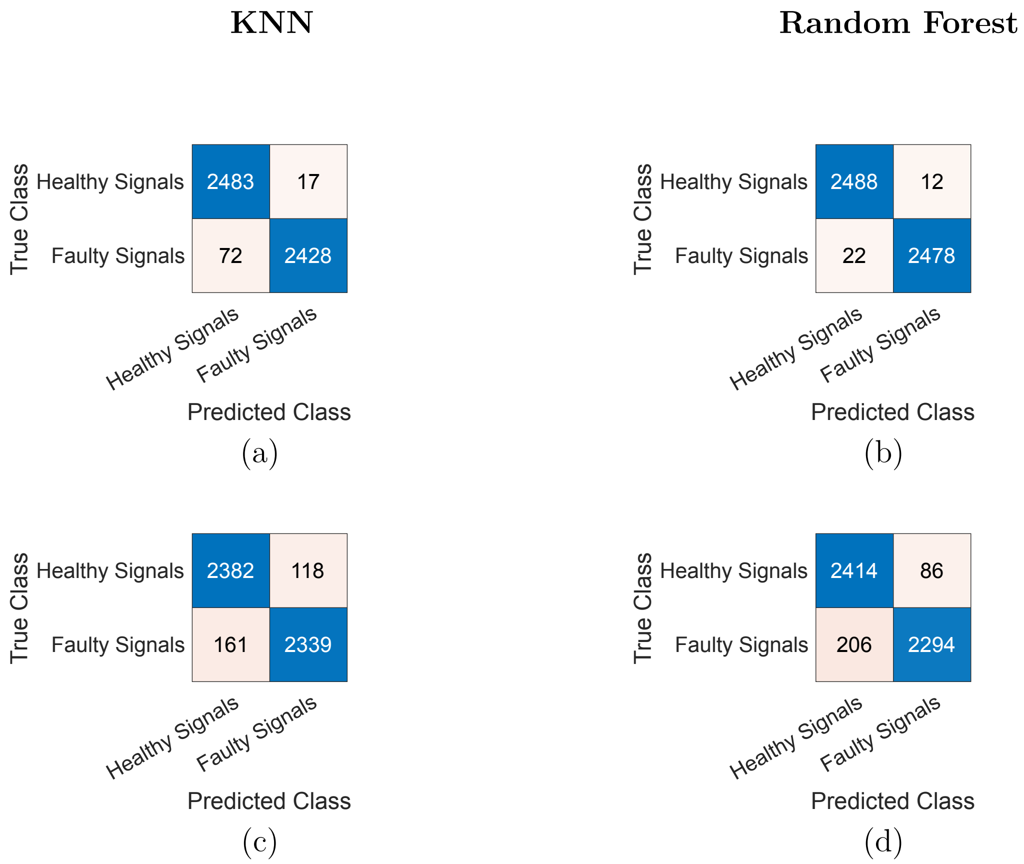

Figure 34: Confusion matrices for FD across two datasets (`KPI_Y` and `KPI_R`), using KNN and Random Forest classifiers. Subfigures: (a) `KPI_Y` with KNN, (b) `KPI_Y` with Random Forest, (c) `KPI_R` with KNN, (d) `KPI_R` with Random Forest.

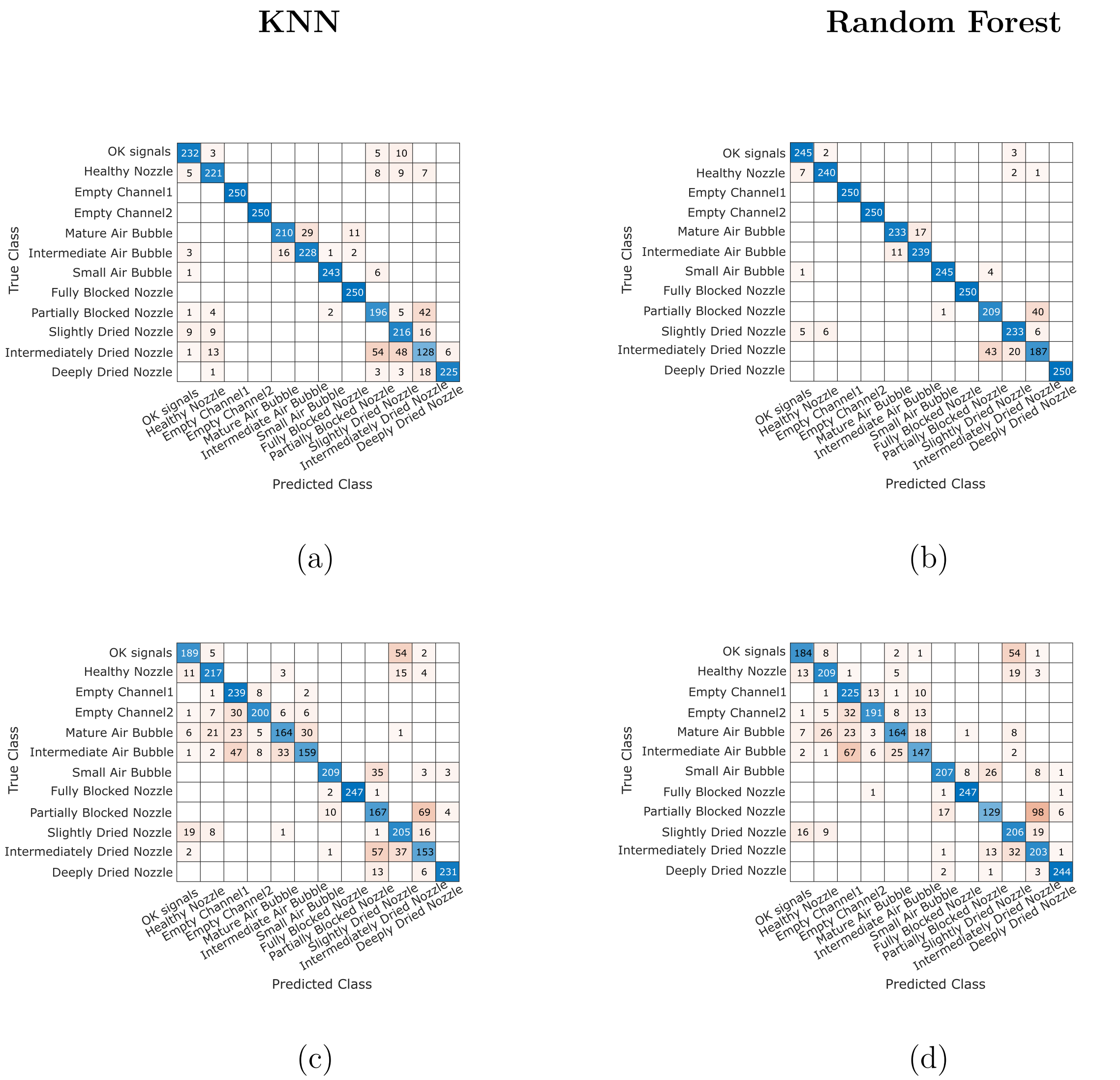

Figure 35: Confusion matrices for FI across two datasets (`KPI_Y` and `KPI_R`), using KNN and Random Forest classifiers. Subfigures: (a) `KPI_Y` with KNN, (b) `KPI_Y` with Random Forest, (c) `KPI_R` with KNN, (d) `KPI_R` with Random Forest.

Based on the results in Table 2, the classifier trained on the `KPI_Y` dataset using the Random Forest algorithm has achieved the highest accuracy in both FD and FI tasks. Therefore, the following analysis focuses on this specific configuration.

In this evaluation, the Healthy class is treated as the negative class, and the Faulty class as the positive class. According to the confusion matrix in Figure 34(b), the model correctly identifies 2488 out of 2500 healthy signals (True Negatives), with 12 misclassified as faulty (False Positives). Among the faulty signals, 2478 are correctly classified (True Positives), while 22 are incorrectly predicted as healthy (False Negatives).

From these results, the model yields an F1-score of 99.32% for the faulty class, indicating a strong balance between precision and recall. The False Negative Rate (FNR) is 0.88%, and the False Positive Rate (FPR) is 0.48%, suggesting that the classifier rarely misses faults and seldom flags healthy signals incorrectly. Overall, the results confirm consistent classification behavior with a preference for minimizing the risk of undetected faults.

Figure 35(b) shows the confusion matrix for the FI task using the Random Forest classifier on the `KPI_Y` dataset. Corresponding performance metrics for each class are presented in Table 10.

Fault Class	**Accuracy (%)**	**F1-score (%)**	**FNR (%)**	**FPR (%)**
OK signals	98.00	96.46	2.00	5.04
Healthy Nozzle	96.00	96.38	4.00	3.23
Empty Channel 1	100	100	0.00	0.00
Empty Channel 2	100	100	0.00	0.00
Mature Air Bubble	93.20	94.34	6.80	4.51
Intermediate Air Bubble	95.60	94.47	4.40	6.64
Small Air Bubble	98.00	98.79	2.00	0.41
Fully Blocked Nozzle	100	100	0.00	0.00
Partially Blocked Nozzle	83.60	82.61	16.40	18.36
Slightly Dried Nozzle	93.20	91.73	6.80	9.69
Intermediately Dried Nozzle	74.80	77.28	25.20	20.09
Deeply Dried Nozzle	100	100	0.00	0.00

Table 10: Performance metrics per fault class using the `KPI_Y` dataset and Random Forest classifier. Metrics are based on the confusion matrix in Figure 35(b) and correspond to the results in Table 2.

Table 10 presents the classification performance across all fault categories. Accuracy values exceed 93.00% for most classes, with perfect isolation for several fault types, including **Empty Channels**, **Fully Blocked Nozzles**, and **Deeply Dried Nozzles**.

For more subtle faults, including *Partially Blocked* and *Intermediately Dried Nozzles*, performance declines moderately, with F1-scores of 82.61% and 77.28%, respectively. Still, the model maintains useful performance levels with reasonably low false detection rates.

As discussed in Section 3.3.1, CPP prioritizes minimizing false negatives, i.e., avoiding missed faults, even at the cost of a higher false positive rate. This is based on visual print impact:

- A false negative may result in a white or light-colored line.

- A false positive may result in a slightly darker line.

In practice, darker lines tend to be less noticeable and less disruptive to print quality than lighter ones. As shown in Table 10, half of the fault classes with non-zero FPR and FNR exhibit lower false negative rates, reflecting the system's preference for conservative fault detection in support of print quality.

C Confusion Matrices for Real-World Dataset Classification

This section presents the confusion matrices for both FD and FI tasks based on real-world signal data. These matrices correspond to the accuracy values reported in Table 7 and provide a detailed view of classifier performance across different datasets and classification methods.

The results are shown for both raw signal features (`KPI_Y_Real`) and residual signal features (`KPI_R_Modified_Real`), using two classification methods: KNN and Random Forest.

KNN **Random Forest**

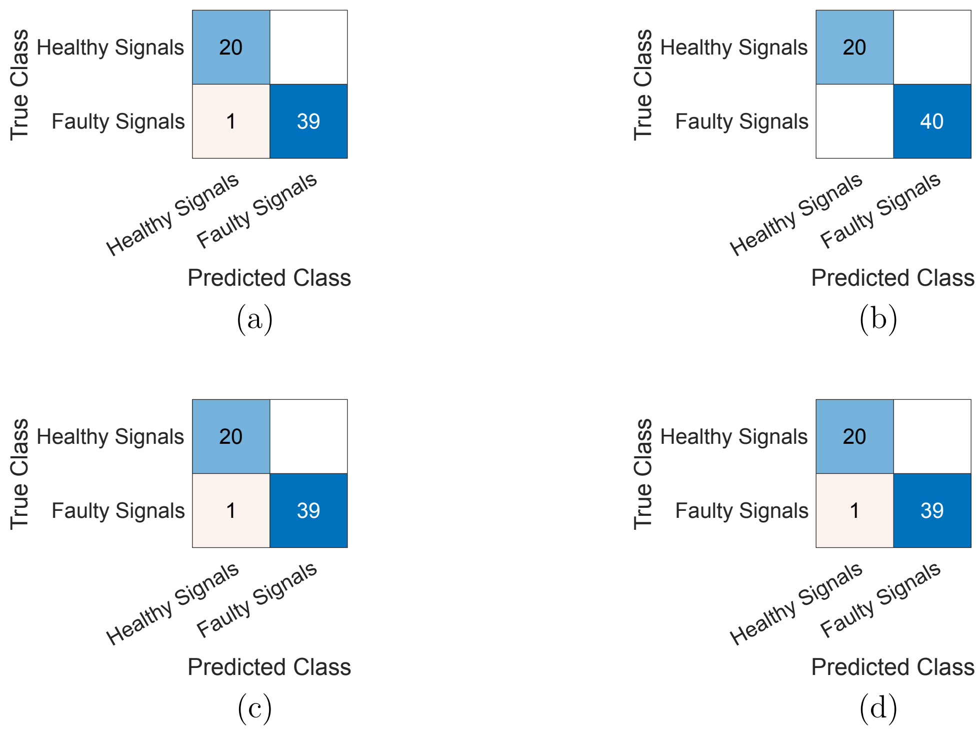

Figure 36: Confusion matrices for FD using real-world data. Results are shown for raw signal features (`KPI_Y_Real`) and residual signal features (`KPI_R_Modified_Real`), using both KNN and Random Forest classifiers. Subfigures: (a) KNN on `KPI_Y_Real`, (b) Random Fores on `KPI_Y_Real`, (c) KNN on `KPI_R_Modified_Real`, (d) Random Fores on `KPI_R_Modified_Real`.

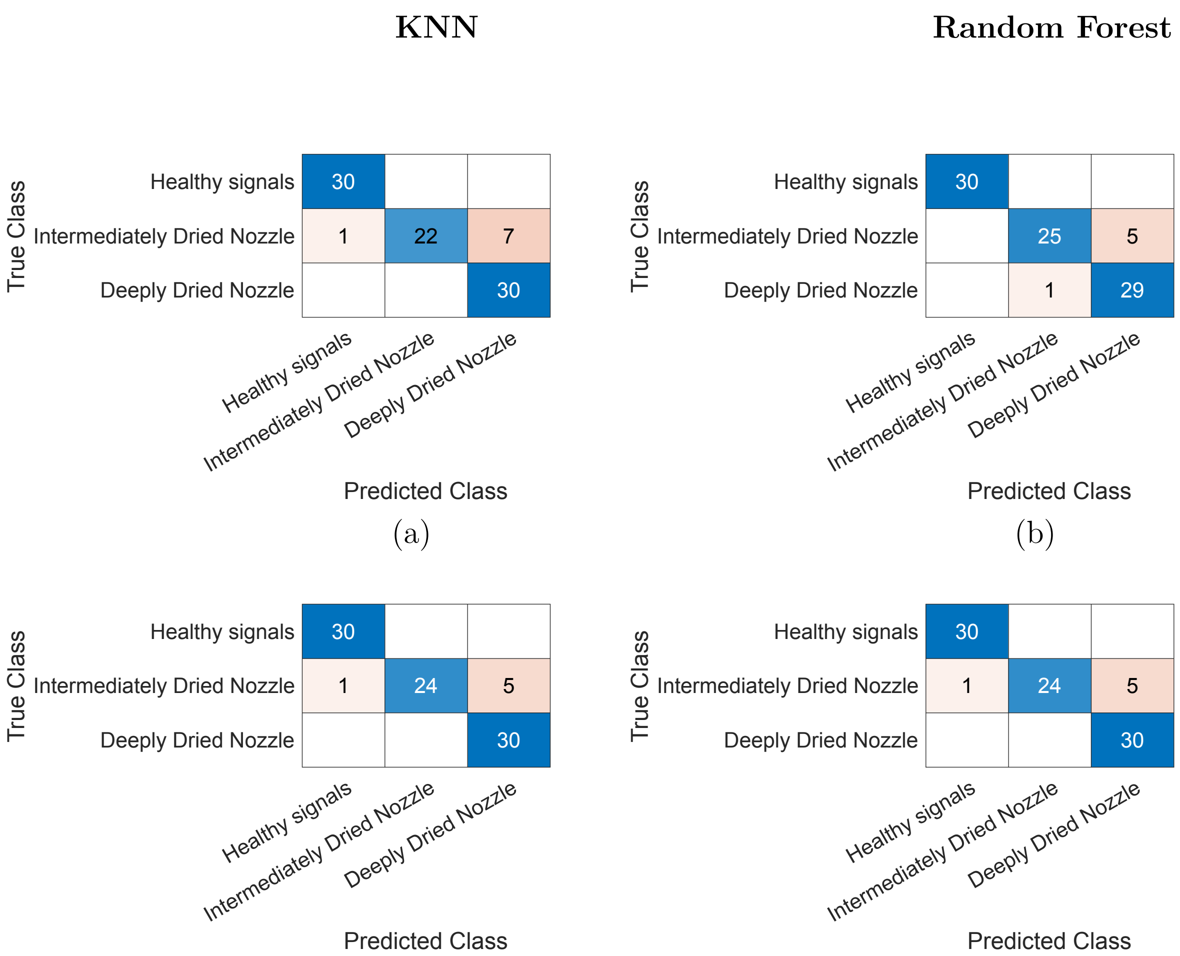

(a) (b) (c) (d)

Figure 37: Confusion matrices for FI using real-world data. Results are shown for raw signal features (`KPI_Y_Real`) and residual signal features (`KPI_R_Modified_Real`), using both KNN and Random Forest classifiers. Subfigures: (a) KNN on `KPI_Y_Real`, (b) Random Fores on `KPI_Y_Real`, (c) KNN on `KPI_R_Modified_Real`, (d) Random Fores on `KPI_R_Modified_Real`.

D Frequency Spectrum Analysis of Fault Classes

This appendix provides additional frequency spectra and plots that support the analysis presented in Section 3.4.3. These visualizations highlight the spectral differences between raw and residual signals for selected fault classes, helping to explain the observed variations in classification performance.

D.1 Empty Channel 1

To investigate the reduced classification performance of the residual-based dataset for the *Empty Channel 1* fault, its FFT spectra in both datasets are analyzed. Figures 38 and 39 show the frequency-domain representations of the raw and residual signals.

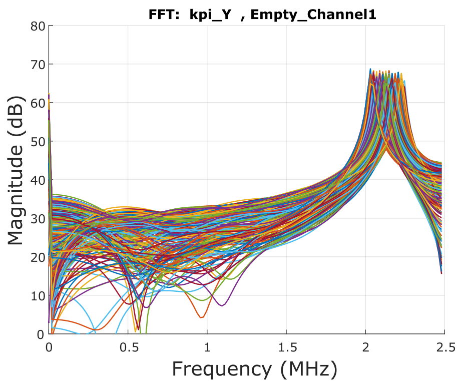

Figure 38: FFT spectrum of `KPI_Y` signals for Empty Channel 1 fault class.

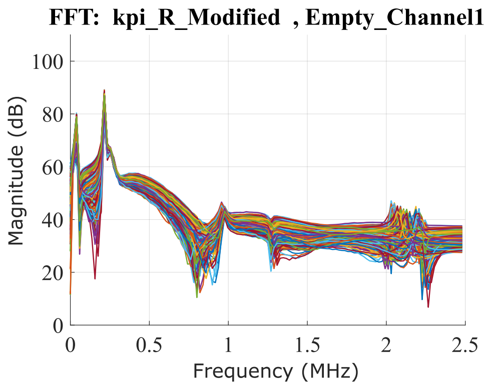

Figure 39: FFT spectrum of `KPI_R_Modified` signals for Empty Channel 1 fault class.

Table 11 compares the dominant frequency peaks of both datasets to the known fault frequency.

Fault classes	Frequencies (kHz)
Empty Channel 1	2124.400
Raw data	[2031.250 , 2246.090]
Residual	214.844

Table 11: Dominant frequency peaks for Empty Channel 1 fault class in raw and residual signals.

These results indicate that the dominant frequencies in the raw signals align well with the expected fault frequency, while the residual signals suppress this high-frequency content. The residual filter introduces its own spectral characteristics, which dominate the resulting signal and mask the original dynamics. This spectral distortion explains the poor classification performance observed in the residual-based dataset for this fault.

D.2 Mature Air Bubble

In contrast, the *Mature Air Bubble* fault class is better classified using residual signals. Figures 40 and 41 show the frequency-domain representations for this fault.

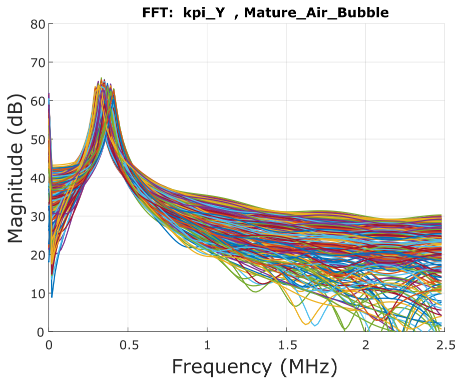

Figure 40: FFT spectrum of `KPI_Y` signals for Mature Air Bubble fault class.

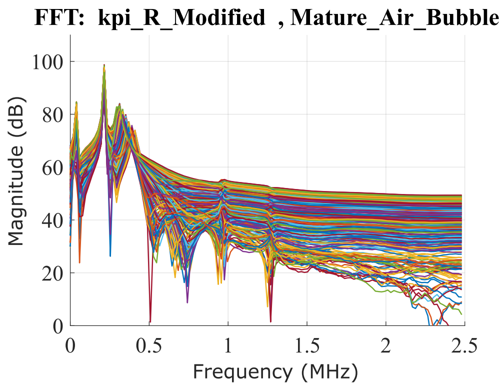

Figure 41: FFT spectrum of `KPI_R_Modified` signals for Mature Air Bubble fault class.

Table 12 provides a comparison of the observed dominant frequency peaks.

Fault classes	Frequencies (kHz)
Mature Air Bubble	357.450
Raw data	[292.969 , 410.156]
Residual	214.800

Table 12: Dominant frequency peaks for Mature Air Bubble fault class in raw and residual signals.

Although the dominant frequency of the residual data shifts slightly, it remains relatively close to the reference value. The raw signal spectrum is broader and less concentrated, which may reduce the separability of this class. These observations support the stronger classification results obtained with the residual-based dataset.

D.3 Fully Blocked Nozzle

The *Fully Blocked Nozzle* fault achieves similar classification performance in both datasets. The FFT spectra shown in Figures 42 and 43 confirm this observation.

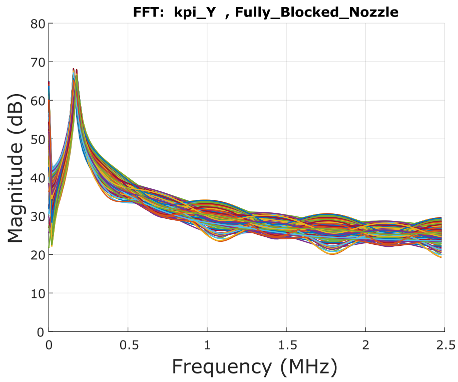

Figure 42: FFT spectrum of `KPI_Y` signals for Fully Blocked Nozzle fault class.

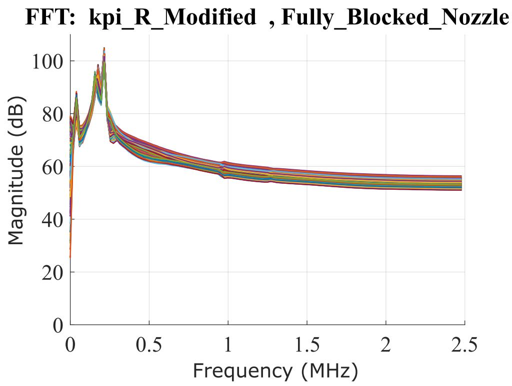

Figure 43: FFT spectrum of `KPI_R_Modified` signals for Fully Blocked Nozzle fault class.

Fault classes	Frequencies (MHz)
Fully Blocked Nozzle	166.350
Raw data	175.781
Residual	214.844

Table 13: Dominant peak Frequencies for Fully Blocked Nozzle Fault Class

The dominant peaks in both the raw and residual signals lie close to the expected fault frequency. This alignment likely contributes to the consistent classification accuracy observed across both datasets for this fault class.

E Taylor Series Expansion for Discretization

This appendix presents the discretization of the faulty continuous-time system matrix A_f^{CT} using a Taylor series expansion. The goal is to justify the approximation method introduced in Section 4.3.4, where only the healthy part of A_f^{CT} is discretized in order to preserve the influence of the fault in a tractable form.

The structure of A_f^{CT} is defined as:

$$\begin{aligned} A_f^{CT} &= \underbrace{\begin{bmatrix} 0 & 1 & 1 \\ -\frac{1}{I_r B_t} & -\frac{R_r}{I_r} & 0 \\ -\frac{1}{I_n B_t} & 0 & -\frac{R_n}{I_n} \end{bmatrix}}_{A_H^{CT}} + \underbrace{\begin{bmatrix} 0 & 0 & 0 \\ 0 & 0 & 0 \\ 0 & 0 & \frac{\Delta R_n}{I_n} \end{bmatrix}}_{\Delta A} \\ &= \begin{bmatrix} 0 & 1 & 1 \\ -\frac{1}{I_r B_t} & -\frac{R_r}{I_r} & 0 \\ -\frac{1}{I_n B_t} & 0 & -\frac{R_n^f}{I_n} \end{bmatrix} \end{aligned} \tag{27}$$

where R_n^f denotes the faulty value of R_n. To approximate the matrix exponential $e^{A_f^{CT} \cdot \mathrm{d}t}$, the Taylor series is applied:

$$e^{A_f^{CT} \cdot \mathrm{d}t} = I + A_f^{CT} \mathrm{d}t + \frac{(A_f^{CT} \mathrm{d}t)^2}{2!} + \cdots + \frac{(A_f^{CT} \mathrm{d}t)^n}{n!} \tag{28}$$

Symbolic computation using MATLAB was performed to expand this expression. For the first-order approximation ($n = 1$), the matrix becomes:

$$e^{A_f^{CT} \cdot \mathrm{d}t} \approx \begin{bmatrix} 1 & \mathrm{d}t & \mathrm{d}t \\ -\frac{\mathrm{d}t}{B_t I_r} & 1 - \frac{R_r \mathrm{d}t}{I_r} & 0 \\ -\frac{\mathrm{d}t}{B_t I_n} & 0 & 1 - \frac{R_n^f \mathrm{d}t}{I_n} \end{bmatrix} \tag{29}$$

In this form, R_n^f appears only in the $(3, 3)$ entry, indicating that the fault influence remains localized when using the first-order expansion.

For a second-order approximation ($n = 2$), the result becomes:

$$e^{A_f^{CT}\cdot \mathrm{dt}} \approx \begin{bmatrix} 1-\frac{\mathrm{dt}^2(I_r+I_n)}{2B_tI_nI_r} & \mathrm{dt}-\frac{R_r\mathrm{dt}^2}{2I_r} & \mathrm{dt}-\frac{R_n^f\mathrm{dt}^2}{2I_n} \\ -\frac{\mathrm{dt}(2I_r-R_r\mathrm{dt})}{2B_tI_r^2} & 1-\frac{I_r(\mathrm{dt}^2+2B_tR_r\mathrm{dt})-B_tR_r^2\mathrm{dt}^2}{2(B_tI_r)^2} & -\frac{\mathrm{dt}^2}{2B_tI_r} \\ -\frac{\mathrm{dt}(2I_n-R_n^f\mathrm{dt})}{2B_tI_n^2} & -\frac{\mathrm{dt}^2}{2B_tI_n} & 1-\frac{I_n(\mathrm{dt}^2+2B_tR_n^f\mathrm{dt})-B_t{R_n^f}^2\mathrm{dt}^2}{2(B_tI_n)^2} \end{bmatrix} \tag{30}$$

At this order, R_n^f appears in multiple entries: $(1,3)$, $(3,1)$, and $(3,3)$, demonstrating that higher-order terms distribute the fault effect throughout the matrix in a nonlinear manner. This distribution complicates the separation of fault dynamics from the nominal system, making the regression-based structure less transparent.

This observation motivates the use of an approximation approach that isolates the fault term. Specifically, the fault-related contribution ΔR_n is separated from the matrix exponential as follows:

$$e^{A_f^{CT}\cdot \mathrm{dt}} \approx \underbrace{e^{A_H^{CT}\cdot \mathrm{dt}}}_{I+A_H^{CT}\mathrm{dt}+\frac{(A_H^{CT}\mathrm{dt})^2}{2!}+\cdots+\frac{(A_H^{CT}\mathrm{dt})^n}{n!}} + \underbrace{\begin{bmatrix} 0 & 0 & 0 \\ 0 & 0 & 0 \\ 0 & 0 & \frac{\Delta R_n}{I_n}\cdot \mathrm{dt} \end{bmatrix}}_{\Delta A} \tag{31}$$

This formulation retains all relevant terms in the Taylor expansion of the healthy system matrix A_H^{CT}, while explicitly preserving the fault structure in a linear and interpretable form. As a result, it supports a clearer implementation of the fault estimation framework, as expressed by:

$$\dot{x} = Ax + B_f E(x) f_m \tag{32}$$

The approximation thereby facilitates a more transparent and tractable design for fault estimation, avoiding the complexity and coupling introduced by higher-order expansions.

F Calculation of Fault Parameter f_m

This appendix presents the derivation of the fault parameter f_m, which quantifies the influence of a change in nozzle resistance, typically due to variations in ink viscosity, on system dynamics. This parameter is used throughout the fault estimation framework to represent the impact of multiplicative faults.

The fault parameter f_m originates from the change in the $(3, 3)$ element of the continuous-time system matrix A in (12), caused by a change in the resistance of the nozzle. It is defined as:

$$f_m = \Delta A(3,3) = -\left(\frac{R_{n2}}{I_n} - \frac{R_{n1}}{I_n}\right) = -\frac{1}{I_n}(R_{n2} - R_{n1}) \tag{33}$$

Here, R_{n1} and R_{n2} denote the resistances of the nozzle in healthy and faulty states, respectively, and I_n is the inertance of the nozzle. The resistance of the nozzle is modeled using the Hagen–Poiseuille equation, which relates the fluid dynamics to the geometry of the nozzle and the viscosity of the ink:

$$R_n = \frac{8\mu L_n}{\pi r_n^4} \tag{34}$$

The parameters are defined as follows:

- μ $[\mathrm{kg} \cdot \mathrm{m}^{-1} \cdot \mathrm{s}^{-1}]$ is the dynamic viscosity of the ink.
- L_n [m] is the length of the nozzle.
- r_n [m] is the radius of the nozzle.

The inertance of the nozzle is calculated using a modified version of the standard inertance formula, which includes a correction term $\frac{\pi}{4} r_n$. This correction accounts for the short length of the nozzle compared to that of an ideal cylindrical tube, for which the basic inertance expression is typically derived. This approximation has been adopted by Canon Production Printing to provide a more accurate estimate of the nozzle inertance.

$$I_n = \rho \cdot \left(\frac{L_n + \frac{\pi}{4} r_n}{\pi r_n^2} \right) \tag{35}$$

The parameter ρ [$\mathrm{kg \cdot m^{-3}}$] represents the density of the ink. Substituting the expressions for R_n and I_n into the definition of f_m yields:

$$f_m = -\frac{1}{I_n}(R_{n2} - R_{n1}) \quad = -\frac{\pi r_n^2}{\rho(L_n + \frac{\pi}{4} r_n)} \cdot \frac{8L_n}{\pi r_n^4} \cdot (\mu_2 - \mu_1) \quad = -\underbrace{\frac{8L_n}{\rho(L_n + \frac{\pi}{4} r_n) \cdot r_n^2}}_{\alpha} \cdot \Delta\mu \tag{36}$$

Here, $\Delta\mu = \mu_2 - \mu_1$ denotes the change in ink viscosity due to a drying fault. Using the provided physical and geometric parameters, the fault parameter can be illustrated as follows:

$$f_m = -\alpha \cdot \Delta\mu \quad [\mathrm{s^{-1}}] \tag{37}$$

This final expression indicates that f_m is linearly dependent on the change in dynamic viscosity. As viscosity increases, representing a drying nozzle, the corresponding rise in resistance alters the system dynamics through the $(3, 3)$ entry of the matrix A.

References

[1] C. P. Printing, “Canon production printing,” 2024, accessed: June 2024. [Online]. Available: https://cpp.canon/about/

[2] D. T. P. 4, “Digital twin project 4,” 2024, accessed: June 2024. [Online]. Available: https://www.digital-twin-research.nl/research/research-project-4/

[3] J. Li, M. Chen, X. Fan, and H. Zhou, “Recent advances in bioprinting techniques: approaches, applications and future prospects,” *Journal of Translational Medicine*, vol. 14, no. 271, pp. 1–13, 2016. [Online]. Available: https://doi.org/10.1186/s12967-016-1028-0

[4] M. J. Uddin, J. Hassan, and D. Douroumis, “Thermal inkjet printing: Prospects

and applications in the development of medicine," *Technologies*, vol. 10, no. 5, p. 108, 2022, submission received: August 2, 2022 / Revised: October 14, 2022 / Accepted: October 17, 2022 / Published: October 21, 2022.

[5] S. Ricci, M. Buonomo, S. Casalini, S. Bonacchi, M. Meneghetti, and L. Litti, "High-performance multi-purpose nanostructured thin films by inkjet printing: Au micro-electrodes and sers substrates," *Nanoscale Advances*, 2023, published: February 16, 2023, under Creative Commons Attribution 3.0 Unported Licence.

[6] D. Takagi, W. Lin, T. Matsumoto, H. Yaginuma, N. Hemmi, S. Hatada, and M. Seo, "High-precision three-dimensional inkjet technology for live cell bio-printing," *Ricoh Company Ltd., Healthcare Business Group*, 2023.

[7] B. H. Kim, N. R. Park, and H. H. Shin, "Error detection apparatus of inkjet printer head and error detection method thereof," US Patent Office, Tech. Rep. US8894178B2, November 2014. [Online]. Available: https://patents.google.com/patent/US8894178B2/

[8] M. Mihailovic, T. E. C. Hummel, J. M. M. Simons, H. Veenstra, C. W. M. Venner, and A. A. Khalate, "Error detection apparatus of inkjet printer head and error detection method thereof," US Patent Office, Tech. Rep. US10144215B2, December 2018. [Online]. Available: https://patents.google.com/patent/US10144215B2/

[9] J. M. M. Simons and M. A. Groninger, "Printing apparatus with measuring circuit for diagnosis of condition of each electromechanical transducer," https://patents.google.com/patent/US6682162B2/, January 2004, patent number: US6682162B2.

[10] Y. Zhang, F. Shi, C. Zhang, X. Sheng, Y. Zhong, H. Chong, Z. Yang, and C. Wang, "Detection of avian influenza virus h9n2 based on self-driving and self-sensing microcantilever piezoelectric sensor," *Chinese Chemical Letters*, vol. 34, no. 4, p. 107700, 2023.

[11] A. Ghosh, D. J. Edwards, M. R. Hosseini, R. Al-Ameri, J. Abawajy, and W. D. Thwala, "Real-time structural health monitoring for concrete beams: A cost-

effective 'industry 4.0' solution using piezo sensors," *International Journal of Building Pathology and Adaptation*, vol. 39, no. 2, pp. 283–311, 2020.

[12] H. Elahi, "The investigation on structural health monitoring of aerospace structures via piezoelectric aeroelastic energy harvesting," *Microsystem Technologies*, vol. 27, no. 7, pp. 2605–2613, 2020.

[13] J. Kang, T. Liu, Y. Lu, L. Lu, K. Dong, S. Wang, B. Li, Y. Yao, Y. Bai, and W. Fan, "Polyvinylidene fluoride piezoelectric yarn for real-time damage monitoring of advanced 3d textile composites," *Composites Part B: Engineering*, vol. 245, p. 110229, 2022.

[14] A. Rayegani, M. Saberian, Z. Delshad, J. Liang, M. Sadiq, A. M. Nazar, S. A. H. Mohsan, and M. A. Khan, "Recent advances in self-powered wearable sensors based on piezoelectric and triboelectric nanogenerators," *Biosensors*, vol. 13, no. 1, p. 37, 2023. [Online]. Available: https://www.mdpi.com/2079-6374/13/1/37

[15] S. Pattipaka, Y. M. Bae, C. K. Jeong, K.-I. Park, and G.-T. Hwang, "Perovskite piezoelectric-based flexible energy harvesters for self-powered implantable and wearable iot devices," *Sensors*, vol. 22, no. 23, p. 9506, 2022. [Online]. Available: https://www.mdpi.com/1424-8220/22/23/9506

[16] P. Hacking, "Classification of jetting behavior based on self-sensing piezo actuators," Master's thesis, Eindhoven University of Technology, 2019.

[17] C. van Peijpe, F. Ghanipoor, Y. de Loore, P. Hacking, N. van de Wouw, and P. M. Esfahani, "Fault isolation for the ink deposition process in high-end industrial printers," *arXiv preprint arXiv:2412.07545*, December 10 2024. [Online]. Available: https://doi.org/10.48550/arXiv.2412.07545

[18] C. P. Printing, "Inkjet prints enhanced with scodix ultra and canon expands inkjet portfolio with variopress iv7," *Canon Netherlands Press Centre*, 2021, focuses on Scodix Ultra enhancement and VarioPress IV7 Accessed: June 2024.

[19] ——, "Canon varioprint ix series - high-performance printhead features," *Canon Netherlands Business*, 2024, accessed: June 2024. [Online].

Available: https://www.canon.nl/business/products/production-printers/digital-presses/variopress-iv7/

[20] K.-S. Kwon and W. Kim, “A waveform design method for high-speed inkjet printing based on self-sensing measurement,” *Sensors and Actuators A: Physical*, vol. 140, no. 1, pp. 75–83, 2007. [Online]. Available: https://doi.org/10.1016/j.sna.2007.05.004

[21] A. Fraters, M. van den Berg, Y. de Loore, H. Reinten, H. Wijshoff, D. Lohse, M. Versluis, and T. Segers, “Inkjet nozzle failure by heterogeneous nucleation: Bubble entrapment, cavitation, and diffusive growth,” *Physical Review Applied*, vol. 12, p. 064019, December 2019. [Online]. Available: https://doi.org/10.1103/PhysRevApplied.12.064019

[22] J. de Jong, G. de Bruin, H. Reinten, M. van den Berg, H. Wijshoff, M. Versluis, and D. Lohse, “Air entrapment in piezo-driven inkjet printheads,” *The Journal of the Acoustical Society of America*, vol. 120, no. 3, pp. 1257–1265, 2006. [Online]. Available: https://doi.org/10.1121/1.2227345

[23] Canon, “Print image quality quantitative evaluation technology,” 2022, accessed: June 2024. [Online]. Available: https://global.canon/en/technology/iqq-evaluation-2022.html

[24] H. Reinten, Y. Jethani, A. Fraters, R. Jeurissen, D. Lohse, M. Versluis, and T. Segers, “Resonance behavior of a compliant piezo-driven inkjet channel with an entrained microbubble,” *arXiv*, vol. physics.flu-dyn, Feb 2023, https://doi.org/10.48550/arXiv.2302.12549. [Online]. Available: https://arxiv.org/abs/2302.12549

[25] T. Cover and P. Hart, “Nearest neighbor pattern classification,” in *IEEE Transactions on Information Theory*. IEEE, 1967, vol. 13, no. 1, pp. 21–27.

[26] L. Breiman, “Random forests,” *Machine Learning*, vol. 45, no. 1, pp. 5–32, 2001.

[27] Oce-Technologies, “Method for compensating a failing nozzle,” 2015.

[Online]. Available: https://worldwide.espacenet.com/patent/search/family/052188779/publication/EP2952355A1

[28] P. M. Esfahani and J. Lygeros, “A tractable fault detection and isolation approach for nonlinear systems with probabilistic performance,” *IEEE Transactions on Automatic Control*, vol. 61, no. 3, pp. 633 – 647, 2016.

[29] C. van der Ploeg, M. Alirezaei, N. van de Wouw, and P. M. Esfahani, “Multiple faults estimation in dynamical systems: Tractable design and performance bounds,” *IEEE Transactions on Automatic Control*, vol. 67, no. 9, pp. 4916 – 4923, 2022.

[30] J. Chen and R. J. Patton, *Robust Model-Based Fault Diagnosis for Dynamic Systems*. Springer, 1999. [Online]. Available: https://link.springer.com/book/10.1007/978-1-4471-3970-9

[31] S. X. Ding, *Model-Based Fault Diagnosis Techniques: Design Schemes, Algorithms, and Tools*. Springer, 2013. [Online]. Available: https://link.springer.com/book/10.1007/978-1-4471-4794-0

[32] R. Isermann, *Fault-Diagnosis Systems: An Introduction from Fault Detection to Fault Tolerance*. Springer, 2006.

[33] S. Hui and S. H. Żak, “Observer design for systems with unknown inputs,” *International Journal of Applied Mathematics and Computer Science*, vol. 15, no. 4, pp. 431–446, 2005.

[34] C. van Peijpe, “Fault isolation for the ink deposition process in high-end industrial printers: A master’s thesis,” Master’s thesis, Delft University of Technology, Delft, Netherlands, June 11 2024.